NOVA SCHOOL OF
SCIENCE & TECHNOLOGY

DEPARTAMENT OF
SCIENCE MATERIALS

ANTÓNIO MARIA DE BOTTON CARVALHO MARTINS
BSc in Materials Science and Engineering

EXPLORING ELECTROSPINNING FOR TRIBOELECTRIC APPLICATIONS

MASTER IN MATERIALS ENGINEERING
NOVA University Lisbon
September, 2023

DEPARTAMENT OF
SCIENCE MATERIALS

EXPLORING ELECTROSPINNING FOR TRIBOELECTRIC APPLICATIONS

ANTÓNIO MARIA DE BOTTON CARVALHO MARTINS

BSc in Material Science and Engineering

Adviser: João Paulo Heitor Godinho Canejo
Researcher, CENIMAT|i3N, NOVA University Lisbon

Co-adviser: Ana Catarina Bernardino Baptista
Researcher, CENIMAT|i3N, NOVA University Lisbon

Examination Committee:

Chair: João Paulo Borges,
Associate Professor with Habilitation, NOVA University Lisbon

Rapporteurs: Maria Helena Godinho,
Associate Professor with Habilitation, NOVA University Lisbon

Adviser: João Paulo Heitor Godinho Canejo
Researcher, CENIMAT|i3N, NOVA University Lisbon

Members: Ana Catarina Bernardino Baptista
Researcher, CENIMAT|i3N, NOVA University Lisbon

MASTER IN MATERIALS ENGINEERING

NOVA University Lisbon
September, 2023

Exploring electrospinning for triboelectric applications

ACKNOWLEDGEMENTS

Em primeiro lugar, gostaria de agradecer aos meus orientadores Doutor João Canejo e Doutora Ana Baptista, pela oportunidade de trabalhar e desenvolver este tema ao longo destes meses. Foi um privilégio todo o conhecimento, ajuda, acompanhamento, atenção, disponibilidade e amizade que me ofereceram durante este período. Muito obrigado!

Para além dos meus orientadores, agradeço também à Doutora Susete Fernandes, à Doutora Ana Almeida, à Dona Augusta, ao João Carmo e à Rafaela Rosa pelo conhecimento transmitido e todos os momentos em que a sua ajuda foi essencial para este trabalho. Um agradecimento especial ao Cezar Tipa pelo conhecimento, ajuda e orientação desde o projeto de licenciatura e principalmente pela amizade e momentos de conversa ao longo deste percurso académico. Um agradecimento ao DCM, ao Cenimat e a todos os seus docentes com os quais tive o prazer de aprender, em particular ao Professor Doutor João Paulo Borges pela oportunidade de trabalhar no laboratório 107.

A todos os meus colegas por toda a ajuda, amizade, momentos divertidos e longas conversas durante o almoço. Um agradecimento à Mariana Pestana, por sermos parelha em todos os trabalhos desde o primeiro ano, pela motivação neste tema, pela amizade e por toda ajuda.

Aos meus amigos que estiveram sempre presentes e me ajudaram a crescer na amizade, em especial à minha namorada Joana por todo o carinho e apoio ao longo de grande parte deste meu percurso académico.

Por último, mas não menos importante, agradeço à minha família, à minha mãe Claúdia, ao meu pai António e à minha irmã Leonor pela pessoa que sou, pelo carinho e amizade, pela perseverança e pela disciplina, pelo apoio e todos os sacrifícios que fizeram por mim sempre a visar a minha educação.

Este trabalho enquadra-se no âmbito do projeto "All-Fiber Integrated Photovoltaic Storage Devices for e-Textiles" de referência PTDC/CTM-CTM/1571/2020, financiado por fundos nacionais via FCT, IP-.

"If you want to find the secrets of the universe, think in terms of energy, frequency, and vibration." (Nikola Tesla)

ABSTRACT

In the latest period, the energy crisis is an iterant topic. The world's energy demand and consumption have been on the rise with still a 78.9% of fossil fuels use. However, the transition from fossil fuels to renewable energy sources requires intense resource use.

The triboelectric nanogenerators (TENGs) provide an alternative, sustainable and renewable energy source by converting mechanical energy into electrical power, due to the triboelectric effect. Their flexible, small and lightweight nature allows for applications like self-powered sensors and wearable electronics. This study presents a detailed analysis of electrospun TENGs, as well as the selection of materials, the electrospinning parameters and the triboelectric mechanisms used with 3D printed tools, to study the membrane's greater surface area for triboelectric applications. Furthermore, SEM and FTIR analysis of the electrospun membranes is also displayed.

Electrospun membranes with randomly orientated fibers were characterized for their mechanical, electrochemical and surface properties. Results showed that the best pair of membranes for electrical applications paired PVDF–TRFE and PVP polymers. Furthermore, films, bilayer composite electrospun membranes and bilayer composite films' electrochemical properties were observed. Cellulose derivatives, CA and HPC, were also studied due to their sustainable characteristics. CA was paired with all the studied polymers being in the center between the highest and lowest potential materials. Besides PVP, interesting results were obtained when PMMA and PS were paired with PVDF-TRFE, providing the required data to analyze the electrical performance of both electrospun and films, as well as the bilayer composites.

In conclusion, experimental results exhibited that electrospun TENGs provide superior electrical performance compared to film TENGs due to the larger surface area provided by the electrospun fibers.

Keywords: TENG, Electrospun TENG, Randomly Aligned Electrospun Membranes, Films, FTIR, SEM, Surface Area, Bilayer Composite, Electrospinning, Triboelectric Effect, Triboelectric Mechanisms, 3D Printing.

RESUMO

Num período mais recente, a crise energética é um tema recorrente. A procura e o consumo de energia a nível mundial têm aumentado, registando-se uma utilização de 78,9% de combustíveis fósseis. No entanto, a transição dos combustíveis fósseis para fontes de energia renováveis exige uma utilização intensa de recursos.

Os nanogeradores triboelétricos (TENGs) fornecem uma fonte alternativa, sustentável e renovável de energia, convertendo energia mecânica em energia elétrica, devido ao efeito triboelétrico. A sua natureza flexível, pequena e leve permite aplicações como sensores autoalimentados e eletrónicos vestíveis. Este estudo apresenta uma análise detalhada de TENGs eletrofiados, bem como a seleção de materiais, os parâmetros de eletrofiação e os mecanismos triboelétricos utilizados com ferramentas impressas em 3D, com o objetivo de estudar a maior área superficial da membrana para aplicações triboelétricas. Além disso, a análise SEM e FTIR das membranas eletrofiadas também é exibida.

Membranas eletrofiadas com fibras orientadas aleatoriamente foram caracterizadas pelas suas propriedades mecânicas, eletroquímicas e de superfície. Os resultados mostraram que o melhor par de membranas para aplicações elétricas emparelhava os polímeros PVDF-TRFE e PVP. Além disso, foram observadas propriedades eletroquímicas de membranas de filme, compósitos bicamada eletrofiados e de membranas de filme. Os derivados de celulose, CA e HPC, também foram estudados devido às suas características sustentáveis. CA foi emparelhado com todos os polímeros estudados estando no centro entre os materiais de maior e menor potencial. Além do PVP, resultados interessantes foram obtidos quando o PMMA e o PS foram emparelhados com o PVDF-TRFE, fornecendo os dados necessários para analisar o desempenho elétrico das membranas eletrofiadas e de filme, bem como dos compósitos de bicamada.

Em conclusão, os resultados experimentais mostraram que os TENGs eletrofiados proporcionam desempenho elétrico superior em comparação aos TENGs de filme devido à maior área superficial fornecida pelas fibras eletrofiadas.

Palavras chave: TENG, TENG Eletrofiado, Membranas Eletrofiadas Alinhadas Aleatoriamente, Membranas de Filme, FTIR, SEM, Área de Superfície, Composto Bicamada, Eletrofiação, Efeito Triboelétrico, Mecanismos Triboelétricos, Impressão 3D.

CONTENTS

1 INTRODUCTION 1
1.1 Background 1
1.2 Electrospun Triboelectric Nanogenerator 1
1.3 Triboelectric Effect 3
1.4 Electrospinning 4
2 MATERIALS AND METHODS 7
2.1 Materials 7
2.2 Methods 7
2.2.1 Preparation of polymeric solutions 7
2.2.2 Electrospinning of polymeric solutions 8
2.2.3 3D printed objects 8
2.2.4 Characterization of electrospun membranes and films 8
3 RESULTS AND DISCUSSION 9
3.1 Surface morphology analysis of the electrospun membranes 9
3.2 Chemical analysis of the electrospun membranes 12
3.3 Mechanical characterization of the electrospun membranes 14
3.4 Electrochemical characterization 16
3.4.1 Open Circuit Potential - System behavior and data analysis 16
3.4.2 Open circuit potential – Randomly aligned electrospun membranes 18
3.4.3 Open circuit potential - Film 21
3.4.4 Open circuit potential - Comparative analysis 22
3.4.5 Short circuit current - System behavior and data analysis 23
3.4.6 Short circuit current - Electrospun membranes 24
3.4.7 Short circuit current - Films 25
3.4.8 Short circuit current - Comparative analysis 26
4 CONCLUSIONS 29
REFERENCES 31
A ANNEX 39
A.1 Triboelectric series 39
A.2 Preparation of polymeric solutions 40
A.3 Electrospinning of polymeric membranes and other processes 40

A.4 3D printed objects 42
A.4.1 Manual triboelectric mechanism 42
A.4.2 Gravitational triboelectric mechanism 43
A.4.3 Jigsaw triboelectric mechanism 44
A.4.4 Rotational triboelectric mechanism 45
A.5 Characterization of electrospun membranes and films 45
A.6 Surface morphology analysis of electrospun membranes 46
A.7 Chemical analysis of the electrospun membranes 48
A.8 Mechanical characterization of electrospun membranes 49
A.9 Short circuit current - Electrospun membranes 50
A.10 Short circuit current - Films 51

LIST OF FIGURES

Figure 1.1 — Four mechanisms of TENGs (Adapted from [19]). 4
Figure 3.1 – Surface SEM image of CA electrospun membrane. 9
Figure 3.2 – Surface SEM image of PCL electrospun membrane. 9
Figure 3.3 – Surface SEM image of PS electrospun membrane, with a magnified view of the cross section of the electrospun fiber. 10
Figure 3.4 – Surface SEM image of PMMA electrospun membrane. 10
Figure 3.5 – Surface SEM image of PVA electrospun membrane. 10
Figure 3.6 – Surface SEM image of PVDF electrospun membrane. 10
Figure 3.7 – Surface SEM image of PVDF-TRFE electrospun membrane. 11
Figure 3.8 — Surface SEM image of HPC electrospun membrane. 11
Figure 3.9 — Surface SEM image of PVP electrospun membrane. 11
Figure 3.10 — FTIR spectrums of the nine polymeric membranes 12
Figure 3.11 — Stress – strain curves of the nine polymeric randomly aligned electrospun membranes. 14
Figure 3.12 — Comparison of the obtained stress – strain curves. 15
Figure 3.13 — Charge orientation. (a) with PMMA as counter/reference and working PVDF-TRFE; (b) with PVDF-TRFE as counter/reference and working PMMA. 16
Figure 3.14 — Visual representation of V_{oc} measure. 17
Figure 3.15 — Vertical Contact Type. (a) 1 contact from a height of 7 cm; (b) 3 contacts from a height of 7 cm; (c) 1 contact from a height of 2.5 cm. 17
Figure 3.16 — Visualization of high-frequency contacts. 18
Figure 3.17 — Analysis of different stabilization times with in (a) 20 s and 40 s; (b) 80 s 18
Figure 3.18 — Open circuit potential of randomly aligned electrospun membranes paired with CA. 19
Figure 3.19 — Analysis of PS and PVP membranes paired with PVDF-TRFE. 20
Figure 3.20 — Comparison of (a) single-layer electrospun membranes; (b) bilayer composite electrospun membranes; (c) double-layer electrospun membranes. 20
Figure 3.21 — Analysis of bilayer composite electrospun membranes of (a) PMMA paired with PVDF-TRFE; (b) PVP paired with PVDF-TRFE. 21
Figure 3.22 — Comparison between 50 μm and 200 μm of thickness in films of PMMA and PS paired with PVDF-TRFE. 21
Figure 3.23 — Open circuit potential analysis of films. 22

Figure 3.24 — Comparison of bilayer composite films of (a) PMMA paired with PVDF-TRFE; (b) PVP paired with PVDF-TRFE. 22
Figure 3.25 — Comparison between electrospun membranes and films. 23
Figure 3.26 — Comparison between bilayer composite electrospun membranes and bilayer composite films. 23
Figure 3.27 — I_{sc} measurement of electrospun PMMA paired PVDF-TRFE with (a) one contact every 20 seconds; (b) no contacts and (c) multiple contacts. 24
Figure 3.28 — Comparison of (a) single layer electrospun membranes and (b) bilayer composite electrospun membranes of PVDF-TRFE paired with PMMA and PVP. 25
Figure 3.29 — Short circuit current of 50 µm and 200 µm thickness in films of PMMA and PS paired with PVDF-TRFE. 25
Figure 3.30 — Comparison of (a) single layer films and (b) bilayer composite films of PVDF-TRFE paired with PMMA and PVP. 26
Figure 3.31 — Comparative performance analysis of electrospun and films 26
Figure A.1 — Triboelectric series for different materials [33]. 39
Figure A.2 — Schematic of electrospinning setup (Made with BioRender.com). 39
Figure A.3 — Schematic representation of the bilayer composite electrospun membranes. 41
Figure A.4 — Schematic process representation of the bilayer composite electrospun membranes. 41
Figure A.5 — Schematic process representation of the double layer electrospun membranes. 41
Figure A.6 — Schematic process representation of films by casting. 42
Figure A.7 — Schematic process representation of the bilayer composite films. 42
Figure A.8 — Manual triboelectric mechanism. 42
Figure A.9 — Moving membrane support in the gravitational triboelectric mechanism. 43
Figure A.10 — Static membrane support in the gravitational triboelectric mechanism. 43
Figure A.11 — Support for static and moving membranes in the gravitational triboelectric mechanism. 43
Figure A.12 — Gravitational triboelectric mechanism. 43
Figure A.13 — Moving membrane in the jigsaw triboelectric mechanism. 44
Figure A.14 — Jigsaw triboelectric mechanism. 44
Figure A.15 — Rotatory membrane Moving membrane in the rotational triboelectric mechanism. 45
Figure A.16 — Rotational triboelectric mechanism. 45
Figure A.17 — Optical microscopy image of HPC electrospun fibers. 46
Figure A.18 — Optical microscopy image of PVP electrospun fibers. 47
Figure A.19 — Macroscale pictures of the electrospun membranes, with a) PVDF; b) PVP; c) PMMA; d) PVDF-TRFE; e) PCL; f) CA; g) PVA; h) HPC; i) PS 47
Figure A.20 — Comparison of the values of Young's Modulus, Strain and Ultimate Tensile Strength with standard deviation for the nine randomly aligned electrospun membranes. (a) all electrospun membranes; (b) magnified view. 49
Figure A.21 — Short circuit current of electrospun membranes paired with CA. 50
Figure A.22 — Short circuit current analysis of films. 51

LIST OF TABLES

Table 3.1 — Values of Young's Modulus, Strain and Ultimate Tensile Strength with standard deviation obtained for the produced electrospun membranes 15
Table 3.2 – Obtained values of open circuit voltage and short circuit current for the polymeric pairs of randomly aligned electrospun membranes, polymer films, bilayer composite electrospun membranes and bilayer composite films..... 27
Table A.1 — Preparation of polymeric solutions. 40
Table A.2 — Controlled factors used in the electrospun membranes. 40
Table A.3 — Values of Average Fiber Diameter with standard deviation obtained for the produced electrospun membranes. 47
Table A.4 — Values of Wavenumber and corresponding bonds for the produced electrospun membranes. 48

GLOSSARY

TENG	Device that converts mechanical energy to electrical energy at a nanoscale, through the contact-separation or relative sliding of two materials with opposite polarity.
Electrospun	Manufactured with electrospinning.
Triboelectricity	The phenomenon practiced by the TENG of converting mechanical energy into electrical energy.

.

ACRONYMS

TENG	Triboelectric Nanogenerator.
CS	Vertical contact-separation mode.
LS	Lateral-sliding mode.
SE	Single electrode mode.
FT	Freestanding triboelectric-layer mode.
SEM	Scanning electron microscopy
FAIR	Fourier transform infrared spectroscopy
UTS	Ultimate tensile strength
PLA	Polylactic acid
CA	Cellulose Acetate
DMAc	Dimethylacetamide
PMMA	Poly(methyl methacrylate)
PVA	Polyvinyl alcohol
RPM	Rotations per minute
PVP	Polyvinylpyrrolidone
EtOH	Ethanol
HPC	Hydroxypropyl Cellulose
PS	Polystyrene
DMF	Dimethylformamide
PCL	Polycaprolactone
DCM	Dichloromethane
PVDF	Polyvinylidene fluoride
PVDF-TRFE	Polyvinylidene fluoride-trifluoroethylene
MEK	Methyl Ethyl Ketone

SYMBOLS

V_{oc}	Open-circuit potential
I_{sc}	Short-circuit current
F	Tensile force
L	Elongation
σ	Nominal stress
ε	Nominal strain
L_0	Gage length
E	Young's modulus
$Wt.\%$	Weight percentage
$°C$	Celsius degrees
T_{amb}	Ambient Temperature
h	Height
F	Frequency

1 INTRODUCTION

1.1 Background

In recent years, electricity consumption has been on the rise globally. According to an auto-regressive model developed to predict the consumption of electricity worldwide, is expected growth in its use and demand. This consumption is shown with a linear increasing graphical tendency, predicting the values of 26.4 trillion kWh in 2025 and 28.4 trillion kWh in 2029 [2]. The final energy consumption is influenced by many factors such as economic growth, population growth, energy efficiency improvements and regional weather. Since the recession in 2012, the activity growth has been progressively increasing creating more pressure on energy consumption. The weather is not constant yearly, like the 2012 cold winter that boosted consumption that year. About the energy efficiency gains it is stated that energy efficiency gains over the years are becoming gradually smaller [3].

There are several key points regarding energy consumption and its impact on the environment. It is stated that higher institutional quality leads to a rise in CO_2 and CH_4 emissions. Another factor is that countries with a higher gross domestic product and foreign direct investment tend to increase energy consumption, leading to increased environmental pollution due to the use of fossil fuels. The population growth in urban areas has a direct impact on energy consumption and, following, air pollution, being not related to water pollution [4].

Projections from the World Energy Outlook in 2007 indicated that fossil fuels were going to be the dominant and the primary energy source, being responsible for about 84% of energy demand by 2030. To this day fossil fuels are the most used in energy production worldwide [5]. Renewable energy sources are sustainable resources available to decrease fossil fuel use. According to the Renewables 2023 Global Status Report, the share of fossil fuels and modern renewable energy in the total final energy consumption was 78.9% and 12.6%, respectively [6]. This is a step in the right direction compared to the values of 2007, but at what cost? There are many implications for the environment and energy sustainability from the increasing demand for renewable energy technologies. The production of these products requires an intense extraction of minerals from the earth. A given example is the production of an electric vehicle battery for which is needed 227000 kg of extracted, transported and processed materials. This value is much higher than the 11500 kg of petroleum typically consumed by an internal combustion engine over the lifespan of a conventional car [7].

In current times solar, wind, biomass, geothermal, and hydropower are the main sources of renewable energy [8]. In smaller percentage other sources are included in the renewable energy area, for example, sources that convert kinetic energy into generated electricity. Similar to the wind energy source that converts the mechanical energy generated in the turbine to electricity through a generator, triboelectric nanogenerators harvest energy generated from motion transforming it into electricity without the need for bigger-sized turbines and generators [9], [10].

1.2 Electrospun Triboelectric Nanogenerator

The triboelectric nanogenerators (TENG), on a nanoscale, can provide an alternative, sustainable and renewable source of energy. Based on the triboelectric effect and electrostatic induction, the TENG converts mechanical energy to electrical energy, through the contact-separation or relative sliding of two materials with opposite polarity [11].

TENGs can show features like high power density, mobility and flexibility being possible to use as small-sized wearable devices [12], [13]. Moreover, the material selection of TENGs is versatile, displaying advantages like lightness, stretchability, deformability, permeability, transparency, mechanical compliance, waterproofness, biocompatibility, antibacterial activity and comfort [14], [15]. Another advantage is the use of electrospun nanofibers. Electrospinning is a low-cost process and allows the incorporation of sustainable materials while maintaining the electrical efficiency of TENGs [12], [13]. In the literature, it is stated that the use of electrospinning would increase the electrical performance of several different components due to the high surface area and surface morphology [14], [16]. Yeongjun Kim et al. stated that the use of a polyimide nanofibrous membrane increased the electrical performance of the TENG, due to the enlarged surface area having the advantageous application of charging capacitors [17]. Although the electrical output of TENGs is with high voltage, which is not appropriated for utilization as a power source, it can be used as self-powered sensors, self-lighting shoes and tiles, personal health care monitoring and more small portable power devices [13]–[15].

Aswathy Babu et al. describe in the article the study of piezoelectric polymers such as polyvinylidene fluoride (PVDF) and its copolymers in TENGs. PVDF-TRFE was one of the subjects because of its triboelectric properties, low toxicity, and adaptable mechanical characteristics, provided a great use as a contact material. Electrospinning is becoming a preferred method for the fabrication of TENGs including PVDF-TRFE in their nano fiber production. Besides the use of piezoelectric polymers, a demand for eco-friendly and bio-derived materials is growing. Furthermore, the incorporation of optimized functional materials is allowed via the fibrous structures of electrospinning, expanding the applications of electrospinning. This article demonstrates that nanofiber-based TENGs provide high-volume power density with an 85% of conversion efficiency at a macroscale. The use of electrospun PVDF nanofibers combined with polyamide-6 (PA6) films displayed a peak power density of 130.2 W/m^2 [18].

Chen Luo et al. provide an article on the integration of PVDF (Polyvinylidene Fluoride) and PS (Polystyrene) blends for triboelectric and air filtration properties. In their study was displayed better output performance compared with the TENG prepared by pure PVDF pressing films. The short circuit current, the open circuit voltage and the transferred charge increased 2.27 times, 2.88 times and 3.15 times, respectively, to the values of 11.1 μA, 165.9 V and 53.8 nC. Furthermore, the use of electrospun PVDF and PS polymers, beyond their application in energy harvesting are the air filtration capabilities [19].

Cristobal Garcia et al. in their article demonstrate the study of self-powered pressure sensor based on the triboelectric effect. The TENG was fabricated from electrospun PVDF (Polyvinylidene Fluoride) and PVP (Polyvinylpyrrolidone) fibers and the objective was to explore a real-time pressure sensor. The provided experimental results confirm in the TENG's electrical output an absence of piezoelectricity being attributed to the great electron change between the polymers in their contact surface. The tests using the Dynamic Mechanical Analysis show that the self-powered sensor has a substantial sensitivity with 8.8 mV/Pa in the low-pressure range and 3.9 mV/Pa at higher pressures [20].

The research of Yonkang Bai et al. presents a scientific approach to self-powered sensors and responsive shape memory actuators of cellulose acetate (CA) and carbon nanotubes (CNT). The composite of electrospun CA/CNT paired with PVDF exhibited an open-circuit voltage, short-circuit density, and instantaneous power density of approximately 103.2 V, 7.93 mA/m^2, and 0.74 W/m^2, respectively, being capable of powering 96 LEDs. For the self-powered pressure sensor applications, a sensitivity of 3.03 V/kPa for pressures below 6.8 kPa, and a sensitivity of 0.11 V/Pa for pressures in the range of 6.8 to 65 kPa was displayed [21].

The development of transparent, flexible, and stretchable polymeric multilayers using a combination of Poly(ethylene oxide) (PEO) and Poly(acrylic acid) (PAA) was presented by Habtamu Gebeyehu Menge et al. In this research, a multi-layer TENG created by an assembly of Layer-by-Layer is displayed. The TENG exhibited a high electron donation tendency with triboelectric polarity. A remarkable output performance was displayed with an output voltage of 303 V and a current density of

36.1 mA/m². Moreover, the multilayer film showed great mechanical properties in terms of foldability and stretchability [22].

Despite significant strides in the selection of triboelectric materials, there remains a vast unexplored territory. There is still a need for new material combinations and different variations like the bilayer electrospun composite membranes. This work is no exception, offering a revealing study of randomly aligned electrospun membranes and introducing the bilayer composite electrospun membranes made with nine different polymers and their performance as triboelectric nanogenerators.

The used materials were PVDF-TRFE, PVDF, PCL, HPC, CA, PVA, PMMA, PS and PVP. From the chosen polymers, cellulose was used as a reference for the triboelectric test due to its sustainable properties [23]. Furthermore, in modern energy devices, the use of cellulose is leading in the energy materials role and innovations [24]. The polymers were paired and compared to find the TENG with the best performance with the help of a multimeter and a potentiostat and acquire the values of open-circuit potential and short-circuit current [25], [26]. Also, the lab-produced electrospinning membranes were placed under mechanical and surface examination. Last but not least the electrical properties of the electrospun TENGs were compared with film-based TENGs, as well the introduction of the bilayer composite membranes concept. The next chapters will provide a closer look at the important parameters of the TENGs, the triboelectric effect and the electrospinning method.

1.3 Triboelectric Effect

The term triboelectricity derives from the Greek word *tribos* which means to rub. This phenomenon, also known as static electricity, occurs when charges are generated through contact, and subsequent separation, between two materials of different natures. On each material surface are generated two different types of charge, the consequence of the triboelectric effect. Therefore, by approaching and separating, continuously, the two different materials' charges (with opposite charges) can transfer from one surface to another [27]. This enables the use of mechanical energy to acquire electrical energy that can be applied to daily tasks, a given example are the triboelectric nanogenerators (TENGs) [28] for health monitoring [29], sensor security [30] and energy-generating clothes [31].

In history, different charge transfer mechanisms were proposed and debated. Being an ion transfer or an electron transfer differs according to the application due to the ample material universe. This materials' diversity creates a diversification of contacts, like metal-metal, metal-insulator, metal-polymer, polymer-polymer, inorganic-organic, liquid-solid, and liquid-liquid [32]. Having a considerable diversity of combinations, the charge transfer mechanism is different for the combined pairs. In the materials' universe, they tend to charge positively or negatively according to their contact with the other one. Figure A.1 (available in Annex A.1) presents a series of materials organized according to their triboelectric potential (from positive to negative). The materials closer to the top of the list have a greater tendency to develop positive charges, while those at the bottom of the list are more likely to develop negative charges [33].

A TENG is composed of two distinct stacked triboelectric polymer sheets. One of the sheets is for accepting electrons and the other is for donating electrons. The mechanical energy harvested from the touch and rubbing of the sheets against each other leads to the mechanical deformation of the insulating polymer. As a result, charges are generated on the internal surfaces of the polymer due to the triboelectric effect and electrostatic induction. An electrical potential difference occurs on the electrodes attached to the triboelectric layers, causing an electron flow from the lower to the higher potential sides to achieve equilibrium and the accumulation of induced charges in the electrodes. A continuous deformation of the layers reduces the dipole moment. Consequently, the potential differences between the layers decrease, changing the moving direction of electrons. This electrical phenomenon caused by the electron flow can be used to generate electric current [34]. The TENGs can be used in four different operation modes. These mechanisms represented in Figure 1.1 demonstrate in (a) the vertical contact-separation mode (CS) which the potential and current flow are created by using a per-

pendicular motion to the surface creating a gap between them. In (b) the lateral-sliding mode (LS) uses a parallel rubbing to the interface through a sliding or rotation. Represented in (c) is the single electrode mode (SE) the ground is the reference electrode and has the advantage of harvesting energy without an electric conductor and from objects moving freely. Lastly, in (d), freestanding triboelectric-layer mode (FT), similar to the SE mode, the electrical output is induced, as the interface changes position, in the pair of symmetric electrodes from their asymmetric charge distribution [35].

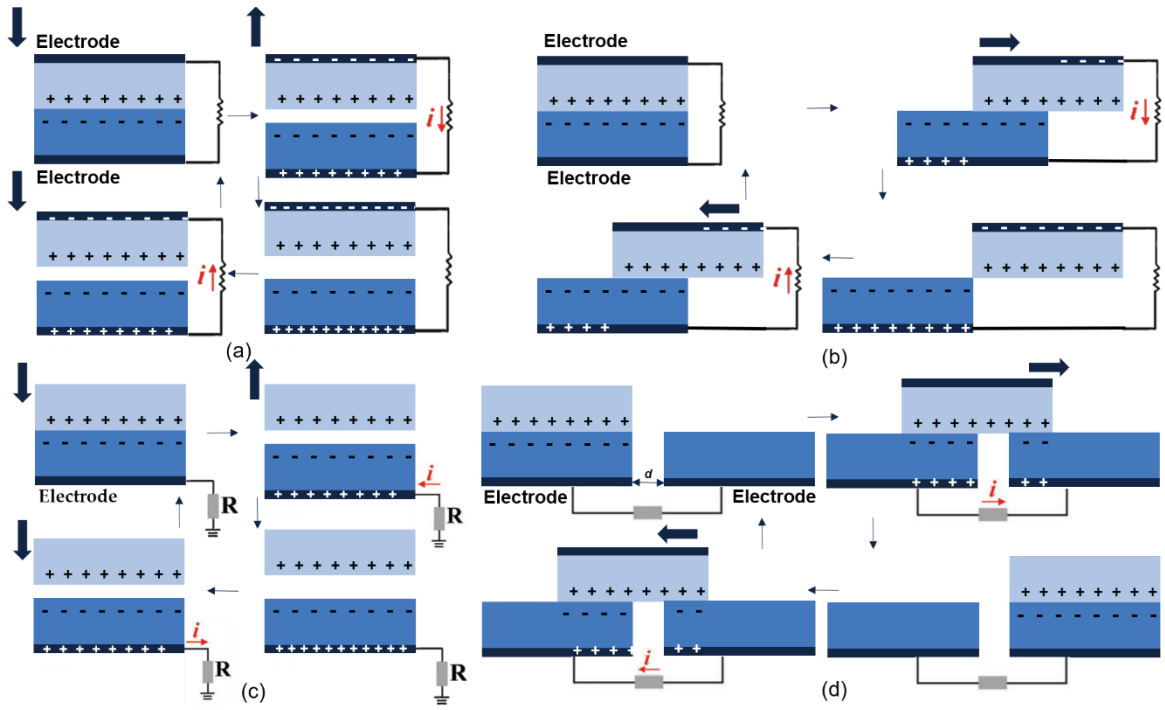

Figure 1.1 — Four mechanisms of TENGs (Adapted from [19]).

In this work, the triboelectric effect of the used TENGs was studied using the contact-separation mode and the lateral-sliding mode. Some 3D printed tools, further shown, were employed in a potentiostat to measure the open-circuit voltage (V_{oc}) and the short-circuit current (I_{sc}). The V_{oc} is the difference of potential between the two electrodes and is measured when the device has no external load and current flow [36]. The I_{sc} is the maximum current flowing in an electrical circuit occurring when the voltage equals zero [37].

1.4 Electrospinning

In order to produce the membranes, electrospinning is one of the most suitable techniques. The membranes are formed by polymeric fibers with diameters at the micro and nanoscale. This technique uses a voltage source to create an electric field between the tip of the needle and the collector where the fibers will be deposited. It presents several advantages, mainly from being an accessible technique with a simple assembly and only a few components [38], [39].

The simplest configuration of equipment used in electrospinning consists of a syringe where the solution will be placed containing the polymer to be deposited, a needle at the end of the syringe, a responsible infusion pump that controls the solution flow rate into the syringe, a metal target or collector where the fibers will be deposited and a voltage source that applies the potential difference between the needle and the target. Toward the creation of an electrical field between the needle and the target, the use of connecting cables is necessary [38], [39]. A schematic representation of the equipment is represented in Figure A.2 (Available in Anex A.1). An electrostatic repulsion force between the

electrostatic charges induced by the electrical field can be created. This occurs with the use of two electrodes, placed at the tip of the needle and in the collector. The polymeric solution initially placed in the syringe is pumped towards the target, forming a drop at the tip of the needle. Due to surface tension, the formed drop has a spherical shape and as a result of the potential difference applied the travelling fiber has the configuration of the Cone of Taylor. In order to avoid a non-uniform fiber, in which the fibers are in liquid form or with droplets, a stretch of the polymer molecules and solvent evaporation must take effect during the stream flight, before reaching the collector [39].

For the effective production of high-quality membranes by electrospinning there are a series of parameters that can and must be controlled, being related to the solution, equipment and environment. Some given examples of these parameters are viscosity, concentration, density, electric conductivity, surface tension, polymer molecular weight, flow, needle diameter and distance to the collector, applied tension, temperature and humidity [40].

The porous membranes made of micro and nano fibers can be obtained, from a wide range of polymeric solutions, and with a high surface area to volume ratio, allowing various applications, for instance in the TENGs. It is a versatile technique since its great mechanical properties, surface topography, fiber orientation and morphology can be easily modified [41]. To study the surface morphology through imaging scanning electron microscopy (SEM) is a suitable technique. The use of Fourier transform infrared spectroscopy (FTIR) is important for chemical analysis [42].

To conclude on the Young's modulus, E, and strength the mechanical properties are studied. The traditional uniaxial tensile tests can be applied to the membranes. Several studies reported that fiber alignment has an impact on elastic modulus. The elastic modulus increased when the fibers were aligned and the test was conducted in a parallel direction to the fibers. The membranes with anisotropic fibers (aligned) can be produced with a rotating metal drum target, while isotropic fibers (randomly orientated) just require a conventional target [42].

In this work a traction machine was used for the nine polymeric randomly aligned electrospun membranes, acquiring the values of the tensile force, F, and the elongation, L. The nominal stress, σ, is defined as [43]:

$$\sigma = \frac{F}{A_0} \tag{1}$$

where the tensile force, F, is divided by the initial cross-section area of the gage section, A_0. The nominal strain, ε, is calculated as [43]:

$$\varepsilon = \frac{\Delta L}{L_0} \tag{2}$$

where the change in gage length, ΔL, is a subtraction between the elongation, L, and the gage length, L_0, (L - L_0). In the stress-strain curve, the point when the material transitions from the elastic deformation to the plastic deformation is named yield strength. Before the material fractures, the ultimate tensile strength (UTS) is the maximum stress the material can withstand. Young's modulus, E, is the slope in the linear region of the strain-stress curve, also known as the elastic deformation [43].

2

MATERIALS AND METHODS

2.1 Materials

Ultrapure water (Míli-Q), Ethanol (Sigma-Aldrich), Acetone (Sigma-Aldrich), Dimethylacetamide (Lab Scan), Methyl Ethyl Ketone (Merck), Dichloromethane (Honeywell), Dimethylformamide (Fisher Scientific), Isopropanol (AGA) were used as solvents.

The polymers used in the preparation of electrospinning membranes were Cellulose Acetate (Sigma-Aldrich, $\bar{M}w$ = 50000 with an average degree of substitution of 1.15), Polyvinyl alcohol (Sigma-Aldrich, $\bar{M}w$ = 95000), Poly(methyl methacrylate) (Sigma-Aldrich, $\bar{M}w$ = 350000), Polyvinylpyrrolidone (Sigma-Aldrich, $\bar{M}w$ = 1300000), Hydroxypropyl Cellulose (Sigma-Aldrich, $\bar{M}w$ = 80000), Polystyrene (Sigma-Aldrich, $\bar{M}w$ = 350000), Polycaprolactone (Sigma-Aldrich, $\bar{M}w$ = 70000-90000), Polyvinylidene fluoride, Polyvinylidene fluoride-trifluoroethylene.

Polylactic acid filament (PLA, Filament2Print) was employed for the preparation of 3D-printed objects. Aluminum foil was used as an electrospinning target and later as an electrode in the electrochemical tests. Parafilm M® was used as an auxiliary in the measurements of the membranes thickness.

2.2 Methods

2.2.1 Preparation of polymeric solutions

The nine polymeric solutions for the electrospinning were prepared by dissolving the polymers in different solvents.

The Cellulose Acetate (CA) solution was prepared with a polymer concentration of 12 wt.% and the used solvents were Acetone and Dimethylacetamide (DMAc) with a volume ratio of 2:1, respectively [44]. To prepare a solution of Poly(methyl methacrylate) (PMMA) with 8 wt.%, a ratio of 3:2 of Acetone and DMAc, respectively, was employed [45]. The Polyvinyl alcohol (PVA) solution used a concentration of 0.1 g/ml, used a mechanical stirrer at 330 rpm in ultrapure water at 80 °C to dissolve the polymer [46]. Polyvinylpyrrolidone (PVP) solution was prepared by dissolving 18 wt.% of the polymer in Ethanol (EtOH) [47]. To prepare a solution of Hydroxypropyl Cellulose (HPC) with 15 wt.% Isopropanol was used [48]. The Polystyrene (PS) solution employed a concentration of 0.3 g/ml, and was dissolved in Dimethylformamide (DMF) [49]. Polycaprolactone (PCL) solution was prepared by dissolution of 13 wt.% of the polymer in a ratio of 3:1 of Dichloromethane (DCM) and Dimethylformamide (DMF), respectively [50]. To prepare a solution of Polyvinylidene fluoride (PVDF), 70% (v/v) of DMF was added and magnetically stirred at 70 °C for 24 hours. Later 30% (v/v) of Acetone was added and magnetically stirred at ambient temperature (T_{amb}) for 24 hours [51]. Polyvinylidene fluoride-trifluoroethylene (PVDF-TRFE) solution was prepared with a concentration of 15 wt.% and was dissolved in a ratio of 9:1 of Methyl Ethyl Ketone (MEK) and EtOH, respectively [52]. All polymers with the exception of PVA and PVDF were magnetically stirred at ambient temperature. Table A.1 (available in Annex A.2) provides the simplified requirements for the preparation of the polymeric solutions.

2.2.2 Electrospinning of polymeric solutions

The nine polymeric solutions were used to produce different electrospun membranes.

The production of the membranes was controlled in a closed environment in an acrylic container and the kdScientific infusion pump was used. Two types of needles were employed, the caliber 25 commercial standard plastic for the PCL and PVP membranes, and the stainless-steel multi-needle with 4 needle points for all the other membranes. Furthermore, 2 ml syringes with 2.47 mm of diameter were used. Several factors were monitored for instance the flow rate, the voltage of the voltage source, the distance from the tip of the needle to the target and the humidity. For the PVA and PVP membranes crosslinking was required. The PVA membrane was required to be in the oven for 4 hours at 180 °C, while the membrane demanded 45 minutes in a Vilber Lourmat UV Crosslinker BIO-LINK BLX-254 at 60 J. All the other factors controlled in each polymeric solution are displayed in Table A.2 (available in Anex A.3). Besides the nine membranes individually electrospun with each polymer, four other membranes were made. These four were composite electrospun membranes featuring a bilayer configuration, which had two polymers in the same membrane matrix. The bilayer membranes were composed of PMMA with PVDF-TRFE and PVP with PVDF-TRFE. The other two membranes employed the same polymers but were electrospun in a different order to change the polymer at the surface. Figure A.3 (available in Annex A.3) provides a schematic representation of the bilayer composite electrospun membranes. Using the same polymers, double layer electrospun membranes and polymeric films including the bilayer composites film produced by casting. These production processes are displayed in Figures A.4, A.5, A.6 and A.7 (available in Annex A.3)

2.2.3 3D printed objects

The tools used in the electrochemical characterization were developed in Autodesk Fusion 360 version 2.0.16486. An Ultimaker 3.0 3D printer was provided to print the parts using PLA as filament, employing a 40% infill density and a high-quality printing with extra fine 0.06 mm layer thickness. All the developed parts are available in Annex A.4.

2.2.4 Characterization of electrospun membranes and films

In this study, the mechanical properties, the electrochemical properties, the surface morphology and the chemical analysis of the produced electrospun membranes were characterized. The mechanical properties were analyzed through several tensile tests using a tensile machine (Minimat Firmware 3.1 from Rheometrics Scientific) equipped with a 20 N load cell performed at a speed of 5 mm/s, for the nine polymer membranes. A potentiostat (Gamry Instruments, Interface 1010E) was used to perform the electrochemical tests and specify the values of short circuit current and open circuit voltage of different pairs of electrospun membranes and films. These triboelectric tests were attained in a room with controlled temperature and humidity of 23 °C and 32%, respectively. Also, a multimeter was used to verify the voltage of the membranes under the jigsaw and rotational triboelectric tests, using an electric jigsaw and a laboratory mechanical stirrer, respectively. The surface morphology and average fiber diameter were observed with the use of the microscopy technique, SEM, employing a Regulus8220 from Hitachi. The samples were placed in 4mm disks and later were coated with a 20 nm layer of gold/palladium (80:20) using sputtering equipment. To calculate and measure the average the software ImageJ was employed and 24 measures were performed for each membrane. The observations were performed with an applied voltage of 5 kV to accelerate the electron beam. FTIR (Perkin-Elmer Spectrum Two FTIR Spectrometer) was used for a chemical analysis. Detailed information is available in Annex A.5.

3
RESULTS AND DISCUSSION

In this chapter, the obtained results and respective discussion are exhibited. The combination of results allows a closer look at the mechanical, electrochemical and surface properties of the produced electrospun and films. All the acquired data and its examination show possible new findings in the TENG domain.

3.1 Surface morphology analysis of the electrospun membranes

This section is dedicated to the analysis of the obtained SEM images for the polymeric electrospun membranes. The acquired images from SEM microscopy will be displayed for the nine polymers CA, PCL, PMMA, PS, PVA, PVDF and PVDF-TRFE. Furthermore, the average fiber diameter of each electrospun membrane is also provided. The SEM images for the HPC and PVP electrospun membranes are later available and analyzed due to the existence of melted fibers.

In Figure 3.1, is provided the SEM image for the CA electrospun membrane, which displays an average fiber diameter of 0.635 ± 0.281 µm.

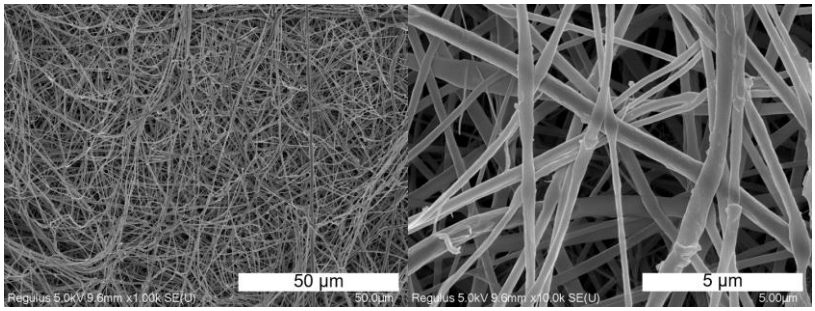

Figure 3.1 – Surface SEM image of CA electrospun membrane.

In Figure 3.2, is provided the SEM image for the PCL electrospun membrane, which displays an average fiber diameter of 1.347 ± 0.766 µm.

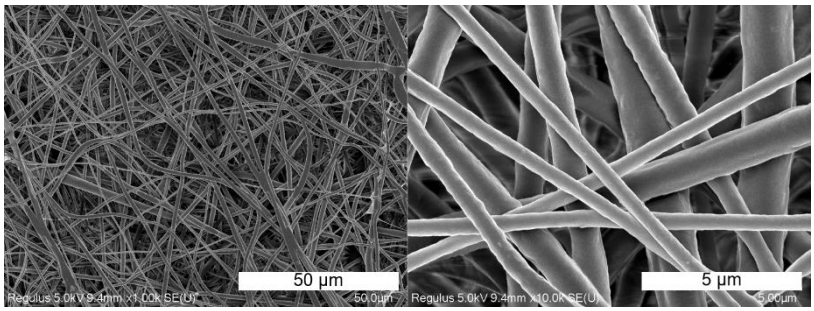

Figure 3.2 – Surface SEM image of PCL electrospun membrane.

In Figure 3.3, is provided the SEM image for the PS electrospun membrane, which displays an average fiber diameter of 3.379 ± 0.184 µm. Also is displayed the cross section of one electrospun fiber of the same polymer exhibiting the porous nature of these electrospun fibers. This porosity of PS fibers that contributes to the increase of the surface area is confirmed by Jinyou Lin et al. in their paper [53].

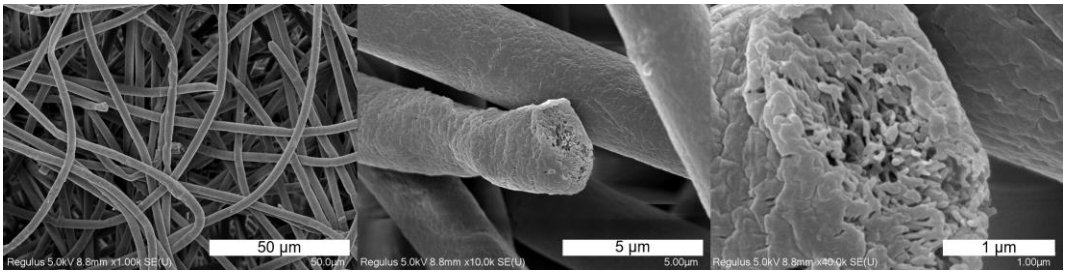

Figure 3.3 – Surface SEM image of PS electrospun membrane, with a magnified view of the cross section of the electrospun fiber.

In Figure 3.4, is provided the SEM image for the PMMA electrospun membrane, which displays an average fiber diameter of 0.593 ± 0.186 µm.

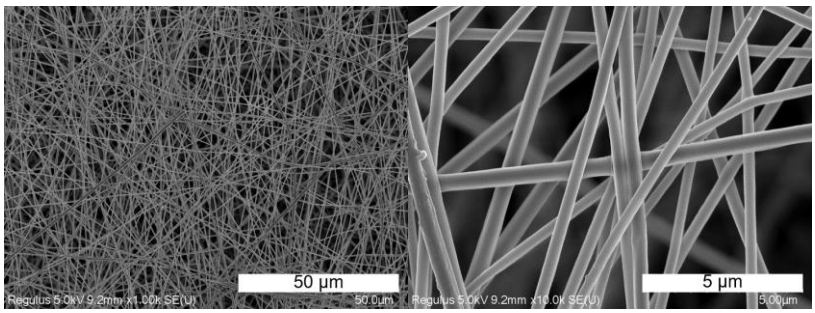

Figure 3.4 – Surface SEM image of PMMA electrospun membrane.

In Figure 3.5, is provided the SEM image for the PVA electrospun membrane, which displays an average fiber diameter of 0.511 ± 0.324 µm.

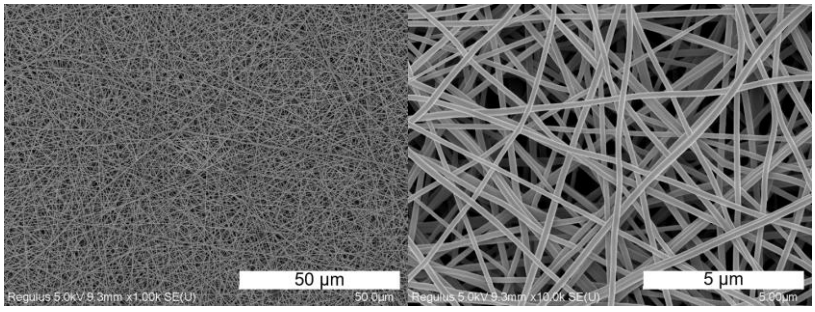

Figure 3.5 – Surface SEM image of PVA electrospun membrane.

In Figure 3.6, is provided the SEM image for the PVDF electrospun membrane, which displays an average fiber diameter of 0.0.597 ± 0.400 µm. This membrane showed irregular fibers that could be caused by the existence of excess solvent that was not evaporated during the electrospinning process. To avoid these fused fibers the electrospinning conditions require optimization.

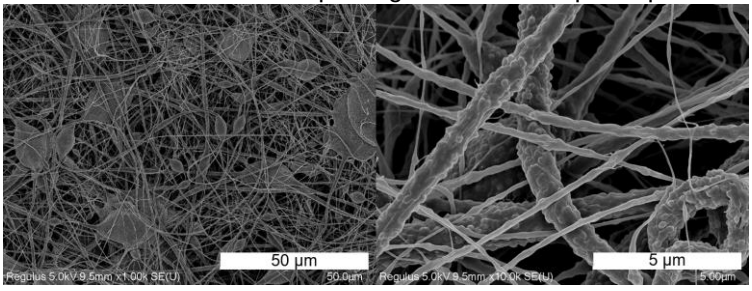

Figure 3.6 – Surface SEM image of PVDF electrospun membrane.

In Figure 3.7, is provided the SEM image for the PVDF-TRFE electrospun membrane, which displays an average fiber diameter of 0.786 ± 0.317 µm.

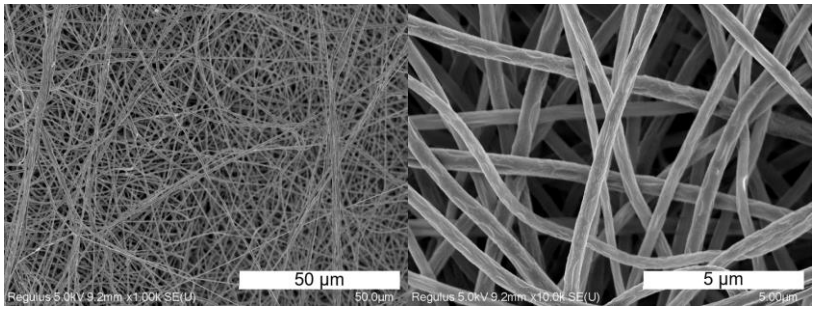

Figure 3.7 – Surface SEM image of PVDF-TRFE electrospun membrane.

In Figure 3.8 is displayed the surface SEM image of HPC electrospun membranes. In this image is visible that the membrane's fibers melted. This can be justified by the solvent excess during the electrospinning process. Moreover, in Figure A.17 (Available in Annex A.6) obtained during the electrospinning process with optical microscopy, is possible to observe that the fibers were presentable at that time and the transition to the melted state could be caused by the air humidity overtime and the lack of cross-linking.

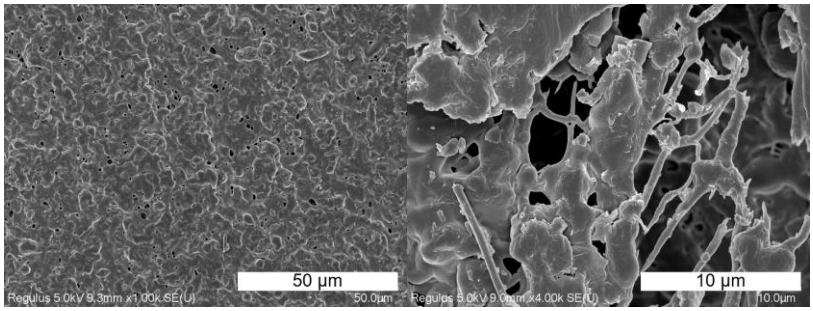

Figure 3.8 — Surface SEM image of HPC electrospun membrane.

In Figure 3.9 is presented the surface SEM image of PVP electrospun membranes. Once again are visible melted fibers in the membrane. In this case, the FTIR spectrum confirmed an excess of solvent, ethanol, in the membrane, justifying the melted fibers. Furthermore, in Figure A.18 (Available in Annex A.6) obtained during the electrospinning process via optical microscopy, is possible to observe that the fibers were presentable at that time. Also, the transition to the melted state could be caused by the air humidity over time, due to poor crosslinking.

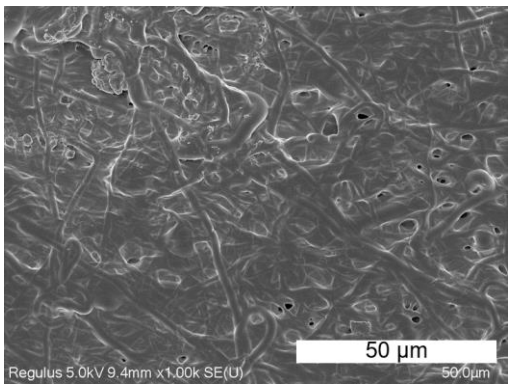

Figure 3.9 — Surface SEM image of PVP electrospun membrane.

In order to compare the values of average fiber diameter with standard deviation obtained for the produced electrospun membranes, table A.3 is displayed in Annex A.6.

3.2 Chemical analysis of the electrospun membranes

The electrospun membranes constitution can be easily identified due to a chemical analysis. In this sub-chapter, this property is studied and discussed, due to the presented data in Figure 3.10. This figure displays nine graphs, one for each polymeric membrane, being obtained through FTIR spectroscopy. In Table A.4, available in Annex A.7, is presented all the wavenumber values and the respective functional groups for each polymer.

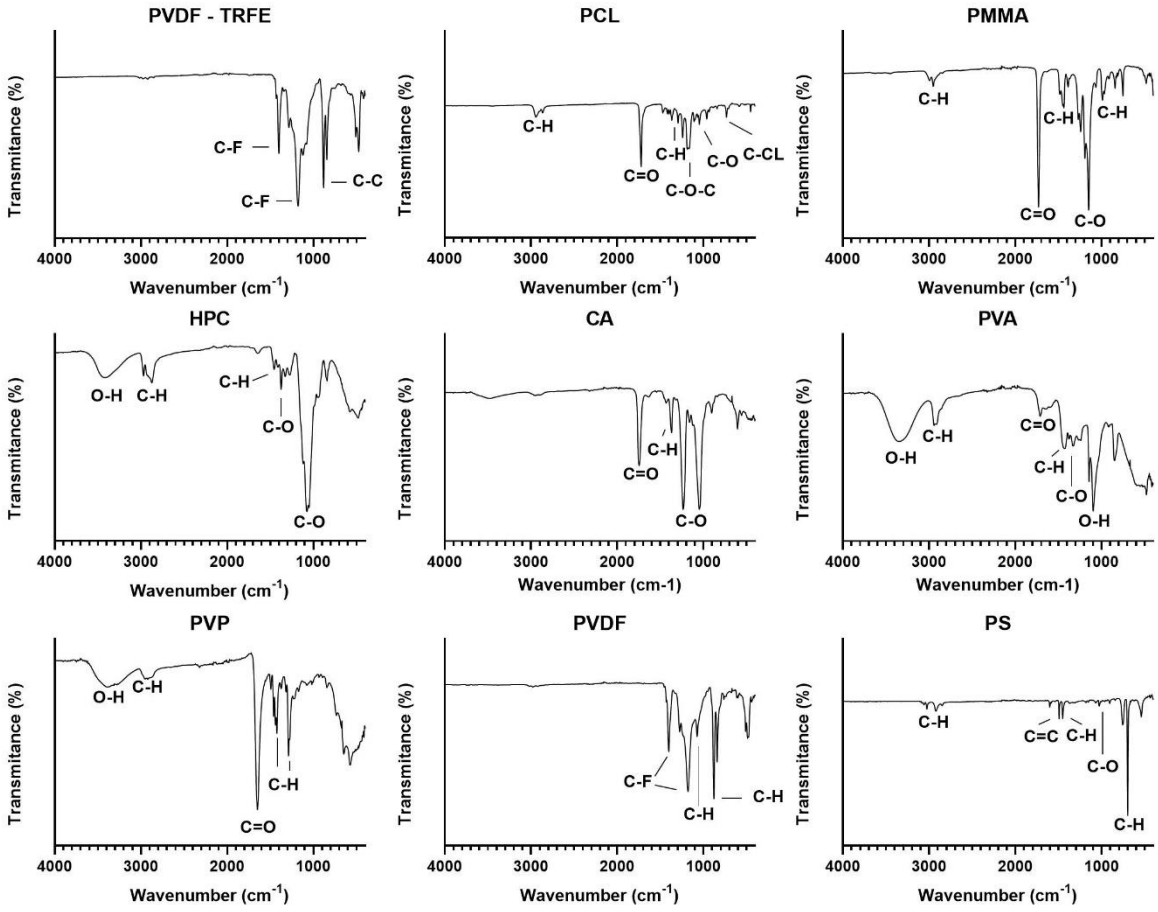

Figure 3.10 — FTIR spectrums of the nine polymeric membranes

PVDF-TRFE dissolved in MEK when examined using FTIR spectroscopy some peaks are identified. Around the 1400 cm^{-1}, 1178 cm^{-1} and 1120 cm^{-1} peaks C-F stretching vibrations are expected, being usually found in fluorinated polymers, in this case PVDF. The peak at 1283 cm^{-1} could be originated from C-F vibrations from the TRFE component. The peak at 881 cm^{-1} could be an indication of vibrations in the C-C bonds. C-H bending vibrations in MEK can justified by the presence of a methyl group (CH_3) in 843 cm^{-1} peak. The last peaks in the 507 cm^{-1} and 473 cm^{-1} regions are likely related to structural vibrations [54]–[56].

The FTIR spectrum of PCL dissolved in DMF and DCM displays several peaks. At 2943 cm^{-1} and 2926 cm^{-1} could represent stretching vibrations of the C-H bonds. The 1723 cm^{-1} peak might be related to the C=O stretching vibration of the carbonyl group in PCL. The 1471 cm^{-1}, 1241 cm^{-1} and

1188 cm^{-1} peaks are related to C-H bending vibrations in the aliphatic chains of PCL [57]. The presence of another carbonyl group (C=O) could be identified in the 1366 cm^{-1} peak verifying the presence of DMF [58]. Also, the 1294 cm^{-1} peak represents a C-O-C stretching vibration in PCL. Moreover, the 1047 cm^{-1} peak could be related to the C-O stretching vibration in PCL's ester group. The presence of DCM can be identified by the C-Cl stretching vibrations in the 732 cm^{-1} peak [59]. Lastly, the 453 cm^{-1} peak is related to structural vibrations in polymers.

PMMA dissolved in a mixture of DMAc and Acetone, with the help of FTIR spectroscopy reveals several peaks. At 2957 cm^{-1}, it showed the presence of C-H stretching vibrations verifying the presence of DMAc and Acetone [60], [61]. At 1731 cm^{-1}, the highlighted peak corresponds to the C=O stretching vibration of the carbonyl group in PMMA. C-H bending vibrations of the PMMA structure are identified at 1488 cm^{-1}, 1437 cm^{-1} and 1195 cm^{-1} peaks. The presence of the C-O stretching vibration in the PMMA ester linkage is suggested by the peak at 1242 cm^{-1}. Furthermore, the 1150 cm^{-1} peak potentially corresponds to the C-O stretching vibration in the PMMA ester group, while the 990 cm^{-1} peak hints at C-H out-of-plane bending vibrations within the PMMA structure. Lastly, failing within the range, the polymer structural vibrations at the 843 cm^{-1}, 751 cm^{-1} and 481 cm^{-1} peaks [62].

HPC combined with Isopropanol provides a FTIR spectrum with various peaks. The hydroxyl (-OH) groups found in both HPC and isopropanol represents O-H stretching vibrations in the peak at 3457 cm^{-1}. At 2974 cm^{-1} and 2882 cm^{-1} the peaks suggest C-H stretching vibrations present in the aliphatic chains of both HPC and isopropanol. The 1457 cm^{-1} peak could be assigned to C-H bending vibrations within the molecular structures of both components. In the 1376 cm^{-1} peak C-O stretching vibrations of the cellulose compound in HPC, are also suggested in the 1079 cm^{-1} peak with presentation also in isopropanol. The last peaks at 841 cm^{-1}, 579 cm^{-1} and 491 cm^{-1} are associated with structural vibrations in polymers [63], [64].

The obtained FTIR spectrum of CA dissolved in a mixture of DMAc and Acetone displays several peaks. The peak located at 1748 cm^{-1} is characteristic of the ester derivate of cellulose, representing a C=O stretching vibration of the carbonyl group. The 1371 cm^{-1} peak could be related to C-H bending vibrations in the cellulose acetate structure, as well as in methyl groups of DMAc [60], [61]. Furthermore, the peak at 1238 cm^{-1} displays C-O stretching vibrations in CA. The 1052 cm^{-1} peak may correspond to C-O stretching vibrations in cellulose acetate, and also in DMAc or acetone molecules [60], [61]. Peaks at 908 cm^{-1} and 607 cm^{-1}, are attributed to lattice or structural vibrations in polymers [65].

PVA dissolved in water exhibits several FTIR spectroscopy peaks. The peak at 3369 cm^{-1} is common in the presence of PVA and water, representing in hydroxyl groups, O-H stretching vibrations. Moreover, the 2943 cm^{-1} peak demonstrates C-H stretching vibrations in the aliphatic chains of PVA. The 1715 cm^{-1} peak is linked to the C=O stretching vibration in PVA. Additionally, the 1437 cm^{-1} peak may be linked to C-H bending vibrations in the molecular structure of PVA or water. The 1334 cm^{-1} peak could represent C-O stretching vibrations in PVA. O-H bending vibrations in water can be found at the 1097 cm^{-1} peak. The last peaks at 851 cm^{-1}, 480 cm^{-1} and 144 cm^{-1}, are associated with structural vibrations in polymers. The peak at 3369 cm^{-1} is indicative of water content in the membrane, being an O-H stretching peak [66], [67].

PVP dissolved with ethanol reveals several distinct peaks in the FTIR spectrum. The peak at 3381 cm^{-1} is common in the presence of PVP and ethanol, representing in hydroxyl groups, O-H stretching vibrations. Furthermore, the 2925 cm^{-1} peak is linked to C-H stretching vibrations in the aliphatic chains of ethanol. The 1650 cm^{-1} peak could represent the C=O stretching vibration of the carbonyl group in PVP. The 1463 cm^{-1} peak may be related to C-H bending vibrations in the molecular structures of PVP and ethanol. The 1423 cm^{-1} peak is associated with the C-H stretching in PVP. The peaks at 650 cm^{-1} and 576 cm^{-1}, are associated with structural vibrations in polymers. The peak at 3381 cm^{-1} is indicative of ethanol content in the membrane, being an O-H stretching peak [68]–[70].

The FTIR spectrum of PVDF dissolved in DMF and Acetone exhibits distinctive peaks. The presence of fluorinated polymers displayed in the peaks at 1403 cm^{-1}, 1276 cm^{-1}, and 1180 cm^{-1},

which are associated with characteristic C-F stretching vibrations in PVDF. The 1073 cm^{-1} peak could represent C-H bending vibrations or other vibrations in DMF or acetone, as well as in the 879 cm^{-1} and 841 cm^{-1} peaks. The last peaks at 510 cm^{-1} and 489 cm^{-1}, are related to lattice or structural vibrations in polymers [71]–[73].

PS dissolved with DMF provides various peaks in the FTIR spectrum. The existence of PS can be confirmed by the peaks at 3000 cm^{-1}, indicating the C-H stretching, and 1601 cm^{-1} of the C=C stretching vibrations in the polymer. Moreover, the peak at 2928 cm^{-1} suggests the existence of aliphatic hydrogen atoms within PS's aliphatic chains. The 1494 cm^{-1} peak represents C-H bending vibrations in PS. Furthermore, the peaks in the 1060 cm^{-1} region, represent C-O bonds in the compound. The 757 cm^{-1} peak is likely associated with vibrations involving C-H bending in PS. Lastly, polymer structural vibrations are observed at 698 cm^{-1} and 542 cm^{-1} peaks [74].

3.3 Mechanical characterization of the electrospun membranes

The stress-strain curves of the nine polymeric randomly aligned electrospun membranes were obtained from all the collected data in the tensile testing. Figure 3.11 shows the acquisition of the stress-strain curves and allows a comparison between electrospun membranes. Regarding the plastic deformation, the PVDF-TRFE, PCL and PS membranes show a substantially bigger plasticity, with a higher value of strain. The CA, PVP and PVDF membranes also exhibit some ductility, not as much as the previous three with a much considerably smaller value of strain. The PMMA, HPC and PVA membranes are the most fragile, fracturing almost right after the elastic deformation.

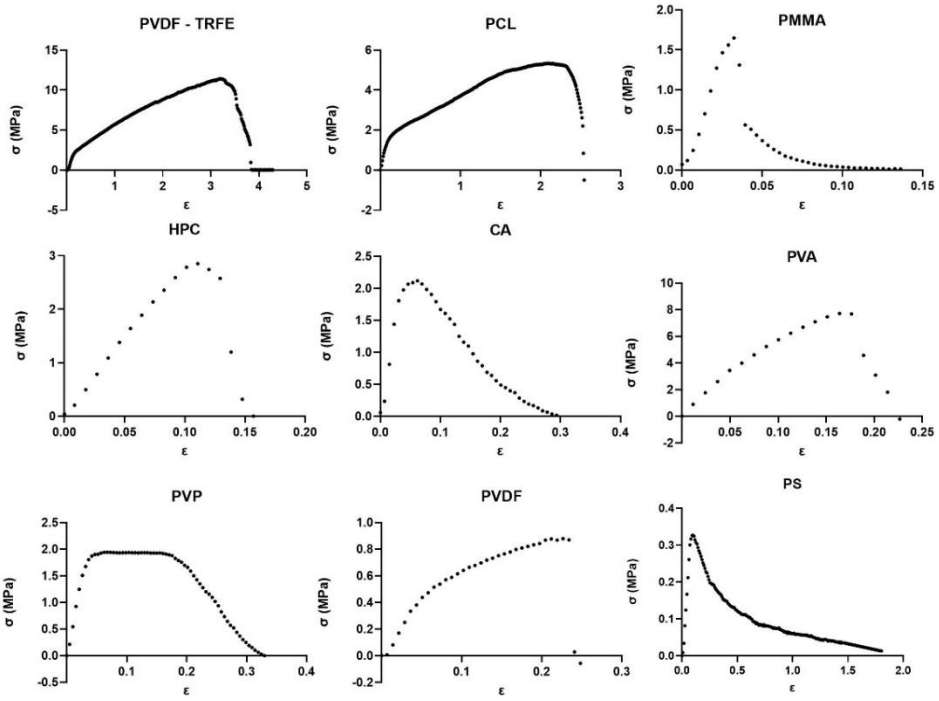

Figure 3.11 — Stress – strain curves of the nine polymeric randomly aligned electrospun membranes.

For a closer comparison of the mechanical properties of the electrospun membranes, Figure 3.12 displays all the membranes in the same graph. In the first graph, Electrospun Membranes, and in graph (a) is easily observed that the membranes of PVDF-TRFE, PCL and PVA have the most substantial ultimate tensile strength values. Graph (b) represents an enlarged version of the main graph and demonstrates the value of UTS for PMMA, HPC, CA and PVP. In a further magnified view, graph (c), the polymers PVDF and PS reveal the least ultimate tensile strength, under 1 MPa.

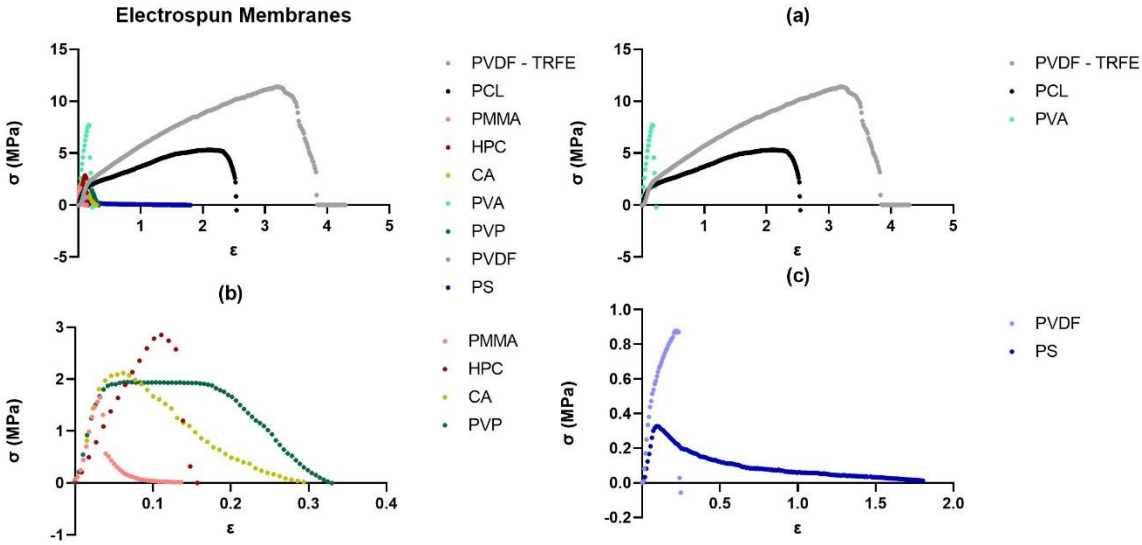

Figure 3.12 — Comparison of the obtained stress – strain curves.

Furthermore, Young's modulus is a mechanical property that can also be analyzed. Table 3.1 and Figure A.20 (Available in Annex A.8) indicate the obtained values regarding Young's modulus, strain and ultimate tensile strength with the respective standard deviation. The membrane which shows a significant value of elastic modulus is the PVP membrane. Although revealing the greatest values of strain, the PVDF-TRFE and PCL membranes, display two of the lowest Young's modulus values, having only at the bottom of the list the PVDF and PS membranes.

In conclusion, the best membranes to handle and prepare for the electrochemical tests of the next section were PCL and PVDF-TRFE due to the great both strain and ultimate tensile strength. Moreover, the PVP, CA and PVA membranes due to their elastic modulus, being stiff membranes are good for the vertical contact triboelectric mode. According to the literature, a long elongation at break was expected for the PVDF-TRFE and PCL membranes and in this work, an even greater elongation was achieved [75], [76]. In terms of Young's modulus for CA and PVP membranes, the values acquired in this work are similar to literature data [77], [78].

Table 3.1 — Values of Young's Modulus, Strain and Ultimate Tensile Strength with standard deviation obtained for the produced electrospun membranes

Polymer	E (MPa)	ε (%)	UTS (MPa)
PVDF-TRFE	16.70 ± 3.06	297 ± 37	11.75 ± 0.91
PCL	17.80 ± 1.50	219 ± 4	5.30 ± 0.10
PMMA	55.00 ± 8.00	6 ± 3	1.99 ± 0.33
HPC	29.58 ± 5.72	12 ± 3	2.70 ± 0.41
CA	69.76 ± 10.95	8 ± 2	2.08 ± 0.20
PVA	63.25 ± 13.27	14 ± 3	5.22 ± 1.92
PVP	72.34 ± 7.22	14 ± 2	2.00 ± 0.30
PVDF	10.49 ± 1.05	23 ± 3	0.87 ± 0.06
PS	7.32 ± 2.14	14 ± 2	0.35 ± 0.08

3.4 Electrochemical characterization

In this section, the electrochemical properties of the triboelectric effect, observed on each sample, are analyzed and discussed. The data was obtained with the assistance of a potentiostat combined with the gravitational triboelectric mechanism, as described in sections 2.2.4 and A.5. The open circuit potential and the short circuit current are divided into sub-sections to examine the electric behavior of the randomly aligned electrospun membranes, the polymer films, the bilayer composite electrospun membranes and the polymer bilayer composite films.

3.4.1 Open Circuit Potential - System behavior and data analysis

This sub-section is presented to understand the system behavior and data analysis. These open circuit potential tests employed a PMMA and a PVDF-TRFE electrospun membranes. The potentiostat has two electrode contacts, one for the counter and reference membrane and the other for the working membrane. Figure 3.13 provides the data of two different tests that (a) used the membrane of PMMA as counter/reference with a working PVDF-TRFE and (b) used the membrane of PVDF-TRFE as counter/reference with a working PMMA. Is stated in the literature that when separating the membranes, the peak should point downwards. Since the electron flow occurs from the lower to the higher potential membrane, when the contact occurs the peak moves upwards. In conclusion, the current flow in the V_{oc} electrochemical test is visualized with a first peak moving downwards and right after a peak moving upwards represented in graph (a). The counter and reference membrane should be the one with the lowest potential, PMMA, and the working membrane with the higher potential is, PVDF-TRFE.

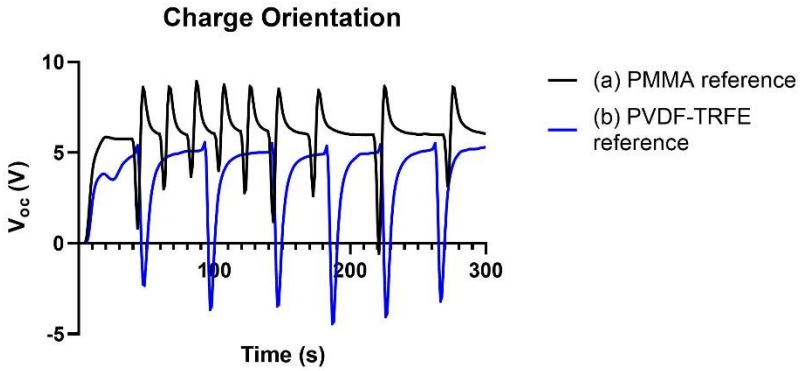

Figure 3.13 — Charge orientation. (a) with PMMA as counter/reference and working PVDF-TRFE; (b) with PVDF-TRFE as counter/reference and working PMMA.

In order to quantify and understand how to measure the value of the open circuit potential, Figure 3.14 is displayed. In the first instance, the membranes are laid in a resting position with the membranes touching each other providing a stable value of V_{oc}, 4V. The stability is interrupted when the membranes are separated with an upward movement of the working membrane, showing a downward peak. The membranes are kept separated and the values return to the stabilization of 4V. In the fourth moment, the working membrane is released and the contact occurs causing the increase of the V_{oc} values. The upward peak takes shape and with the membranes united, later the values return to the stabilization point.

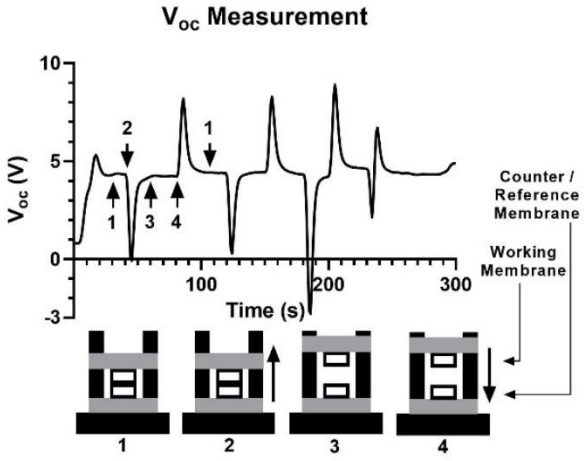

Figure 3.14 — Visual representation of V_{oc} measure.

In the last two upwards peaks of Figure 3.14 the working membrane was separated and immediately dropped into the counter membrane. This mechanism was used in the subsequent provided data. Intending to compare the different pairs of membranes the values of V_{oc} are measured from the stabilization point to the peak maximum value. In Figure 3.14 the average value of V_{oc} is 4V.

As mentioned, the mechanism used to acquire all the data was the gravitational triboelectric mechanism. In this mechanism, the working membrane was elevated and then immediately dropped into the counter/reference membrane. The advantage of this mechanism is to maintain the same velocity and applied force among the electrical tests. Figure 3.15 compares three different vertical contact types. In (a) the working membrane was elevated at a height, *h*, of 7 cm and then dropped while in (c) the membrane was only elevated to a height of 2.5 cm. Trial (b) was similar to trial (a) with the difference that the membrane was elevated and dropped three times in a row (with a frequency, *F*, of 3) before stabilizing. In the literature, was expected that the values of V_{oc} were more substantial in trial (b) then in trial (a) and lastly (c). Contrarily, the values of V_{oc} were greater for trial (a) with trial (b) in the last position, being the reason explained later in Figure 3.16. Consequently, to achieve a careful analysis, all the trials were shaped like trial (a).

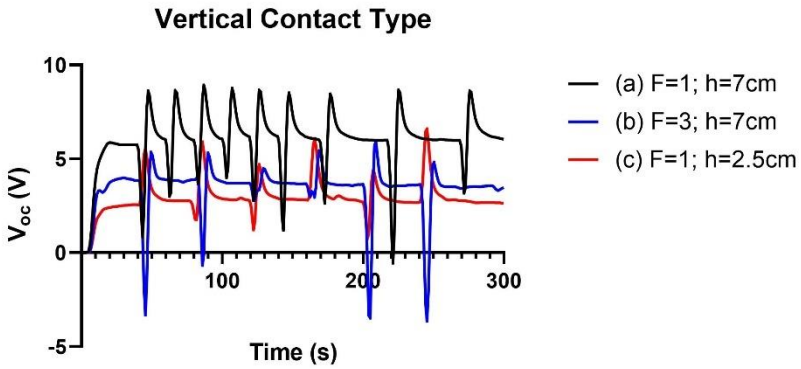

Figure 3.15 — Vertical Contact Type. (a) 1 contact from a height of 7 cm; (b) 3 contacts from a height of 7 cm; (c) 1 contact from a height of 2.5 cm.

Figure 3.16 displays a test using the same electrospun membranes, where the working membranes were lifted and dropped continuously in the periods 40 s to 70 s, 110 s to 140 s and 180 s to 210 s. Similar to trial (b) in Figure 3.15 is impossible to acquire the values of V_{oc}. The reason for this

lies in the fact that the potentiostat is reading the values in a sample time of one second. Since it is a test with high-frequency contacts the potentiostat provides an irregular data reading.

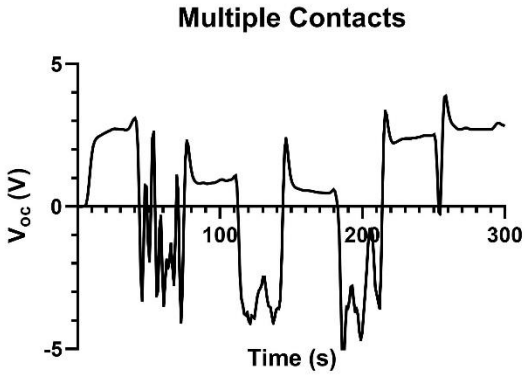

Figure 3.16 — Visualization of high-frequency contacts.

All the open circuit potential tests began with the electrode contacts in short circuit. This means that the first measure from the potentiostat indicated a V_{oc} value of 0V. After the electrode contacts separation, the value of V_{oc} increased and became constant at approximately 2V to 6V, due to the electrostatic exhibited by the membranes. The stabilization time, represented in Figure 3.17, is the time between contacts and longer stabilization times lead to longer periods of constant values of V_{oc}. Graph (a) shows stabilization times of 20 s and 40 s, while graph (b) offers times of 80 s. The average values of V_{oc} are 2.89V and 2.36V, respectively for graphs (a) and (b), concluding that the stabilization time does not affect the measured values.

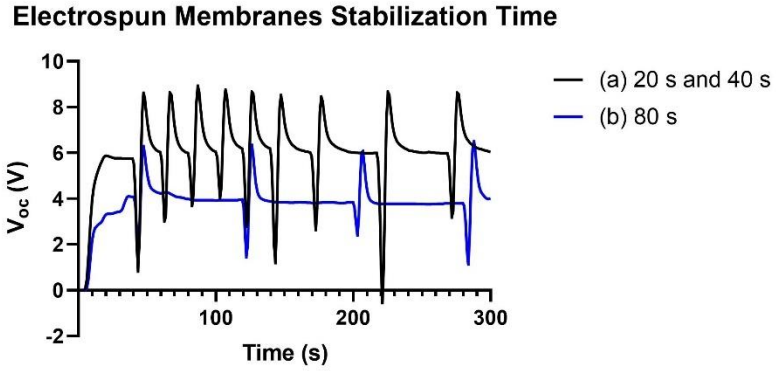

Figure 3.17 — Analysis of different stabilization times with in (a) 20 s and 40 s; (b) 80 s

To conclude in this sub-section, the acquired values and test procedures are not similar to what is expected in literature. In literature, the TENGs' data is obtained using other equipment such as a frequency response analyzer. These devices exhibit V_{oc} values 20 to 30 times greater using high-frequency multiple contacts through the contact-separation mode [79]. In this study, using a potentiostat to study the triboelectric effect of different polymers the gravitational mechanism is applied, where it requires only one contact every 40 seconds and smaller values were obtained.

3.4.2 Open circuit potential – Randomly aligned electrospun membranes

This sub-section is dedicated to the open circuit potential analysis of the produced randomly aligned electrospun membranes and the bilayer composite randomly aligned electrospun membranes.

In pursuit of understanding the polymer's electrochemical behavior, Figure 3.18 is provided. This figure offers eight different graphs in which the CA membrane was used as counter and reference with, as working, the PVDF-TRFE, PVDF, PCL and HPC membranes. In the other four graphs, CA stands as a working membrane with the PMMA, PVA, PS and PVP membranes as counter and reference.

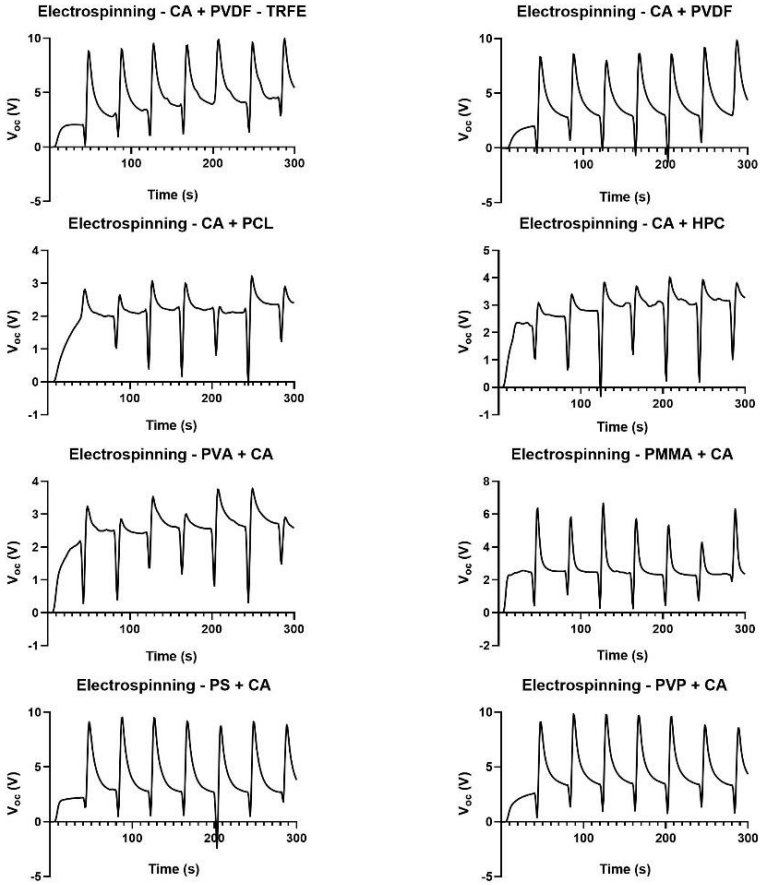

Figure 3.18 — Open circuit potential of randomly aligned electrospun membranes paired with CA.

Since the CA membrane is paired with all the other membranes is possible to compare the potential among the membranes. Using the values of the open circuit potential of each pair, a triboelectric series of the membrane with a higher potential to the membrane with the lowest potential is achievable. The pairs that used CA as counter and reference are the membranes with the higher potential. HPC and PCL achieved V_{oc} values of 0.787 V and 0.792 V, respectively. The membranes with the higher potential are PVDF and PVDF-TRFE reaching values of 5.96 V and 6.84 V.

When CA was used as working, the reference/counter membranes offered the lowest potential, so for these membranes the higher the value of V_{oc} the lower the potential. The PVA and CA pair exhibit a V_{oc} value of 0.85 V, while the PMMA and CA pair display a value of 3.33 V. The lower potential membranes are PVP and PS which, when paired with CA reveal the values 6.35 V and 6.29 V, respectively.

The previous figure allows to assemble a triboelectric series for the randomly aligned electrospun membranes. From the lower potential to the higher potential membranes, the series order is PVP, PS, PMMA, PVA, CA, HPC, PCL, PVDF and PVDF-TRFE.

With the objective of pairing the membranes to obtain the highest values of open circuit potential, Figure 3.19 is presented. The pair with the PS and PVDF-TRFE electrospun membranes offered a

V_{oc} value of 7.12 V. The PVP and PVDF-TRFE pair, as expected provides a value similar to the previous pair of 7.31 V.

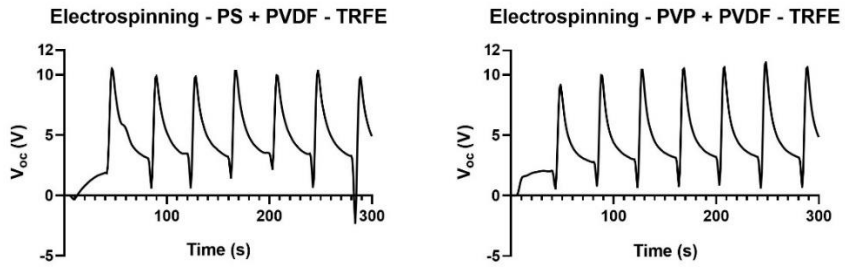

Figure 3.19 — Analysis of PS and PVP membranes paired with PVDF-TRFE.

One of the most relevant studies of this work is the production of bilayer composite membranes and films, and their electrochemical characterization. The bilayer composites are composed of two polymers with different potential electrospun individually, creating a double layer as illustrated in Figure A.3 (Available in Annex A.3). Figure 3.20 provides a comparison of open circuit potential of three different types of electrospun membranes. In (a) the membrane is a common single-layer pair of PMMA and PVDF-TRFE. Graph (b) exhibits a bilayer composite electrospun membrane of PMMA and PVDF-TRFE. In (c) the graph corresponds to a double layer of electrospun membranes, but contrarily to (b) the membranes were electrospun to different targets and later laid on each other.

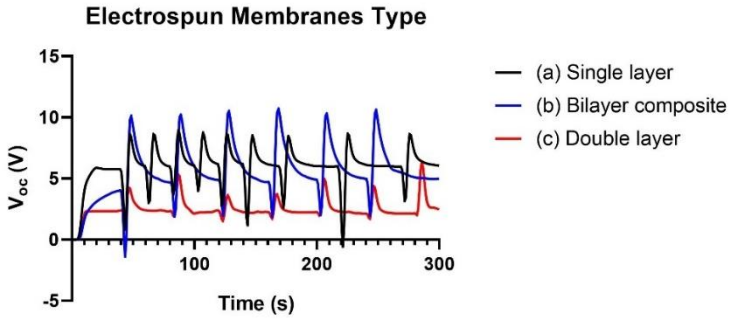

Figure 3.20 — Comparison of (a) single-layer electrospun membranes; (b) bilayer composite electrospun membranes; (c) double-layer electrospun membranes.

The open circuit potential test displayed the values 2.89 V, 5.80 V and 2.44 V, respectively to graphs (a), (b) and (c). The analysis of these results shows a greater value of V_{oc} for the bilayer composite electrospun membrane being two times greater than the other pairs of membranes. This increased value can be justified by the substantially bigger surface area. Having two different potential polymers electrospun on top of the other creates an intertwining between the two polymer layers. In conclusion, apart from the expected contact on the top layers, the impact creates friction among the fibers in the interior layers. In the first instance, the bilayer composite electrospun membranes could contribute to a better performance.

Similar to Figure 3.19 where the pairs of membranes with the highest open circuit potential values were compared, Figure 3.21 examines bilayer composite electrospun membranes in (a) PMMA paired with PVDF-TRFE and in (b) PVP paired with PVDF-TRFE. Despite the pair using PS providing a bigger potential value, PMMA was used instead due to the difficulty of stacking electrospun fibers of PS with other polymers. The pair with the PMMA and PVDF-TRFE electrospun membranes offered a V_{oc} value of 5.80 V. The PVP and PVDF-TRFE pair, as expected provides a value similar to the previous pair of 6.50 V. Despite the V_{oc} value for the PVP and PVDF-TRFE bilayer composite being lower than single layer pair of the same polymers, this bilayer composite provides a greater value than the PMMA and PVDF-TRFE pair, as expected.

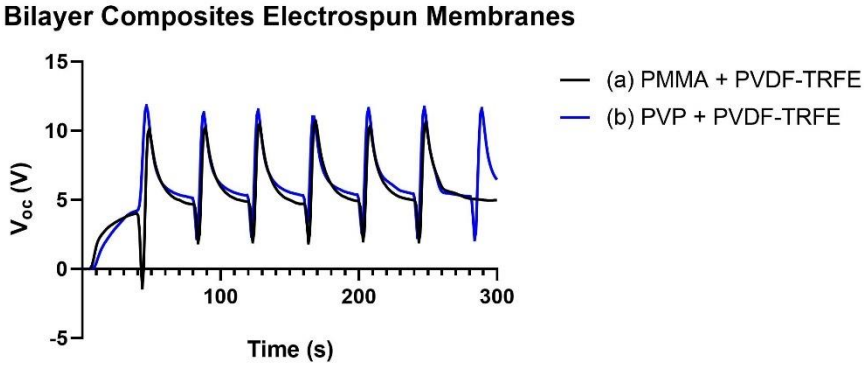

Figure 3.21 — Analysis of bilayer composite electrospun membranes of (a) PMMA paired with PVDF-TRFE; (b) PVP paired with PVDF-TRFE.

3.4.3 Open circuit potential - Film

The open circuit potential of the films will be analyzed in this sub-section. Since the membrane thickness could be controlled, films with 50 µm, 100 µm and 200 µm were made. In order to understand the impact of the film thickness, Figure 3.22 is displayed. This figure compares the open circuit potential value of a pair of films with 50 µm and another pair with 200 µm of thickness. The polymers used were PMMA paired with PVDF-TRFE and PS paired with PVDF-TRFE.

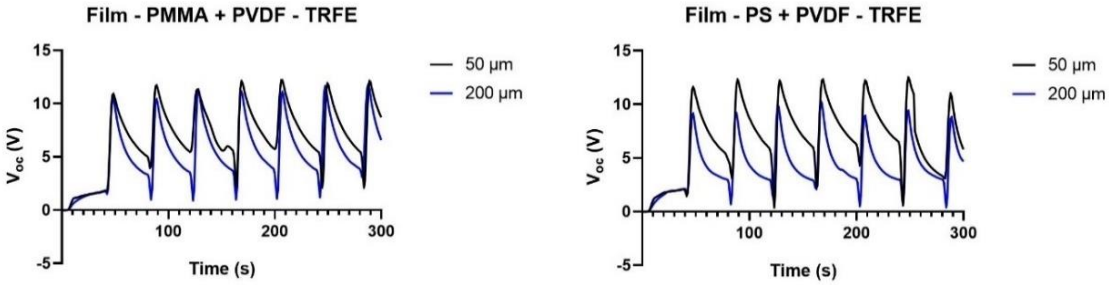

Figure 3.22 — Comparison between 50 µm and 200 µm of thickness in films of PMMA and PS paired with PVDF-TRFE.

For the PMMA and PVDF-TRFE graph, the V_{oc} value is 6.63 V and 7.48 V, for 50 µm and 200 µm, respectively. In the case of the PS and PVDF-TRFE graph, the open circuit potential value is 6.23 V and 6.54 V, for 50 µm and 200 µm, respectively. A four times bigger thickness showed little impact on the open circuit potential values. Since the TENG is measured with a vertical contact mechanism only the surface area has an impact on charge generation, however being PVDF-TRFE a piezoelectric polymer is justifiable for a slightly greater value of V_{oc} for 200 µm films.

Other film pairs were randomly chosen and then tested, which analysis is displayed in Figure 3.23. The acquired open circuit potential values are 5.22 V, 4.55 V and 1.20 V, respectively for the PVP and PVDF-TRFE, PS and PVDF, and, PVA and CA pairs. For the PMMA and HPC pair the produced signal is weaker which is impossible to determine its value. The pairs which show a greater V_{oc} value are the same high potential pairs in the electrospun membranes. In conclusion, the combination of the highest potential membrane with the lowest potential membrane provides a great value of open circuit potential in both film and electrospun membranes.

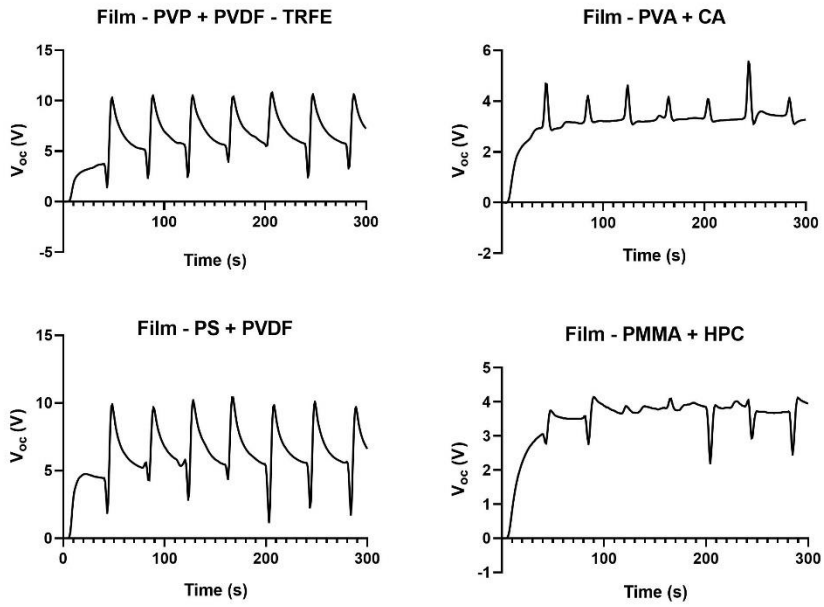

Figure 3.23 — Open circuit potential analysis of films.

Figure 3.24 presents the open circuit potential values acquired for bilayer composite films. These films were composed by PMMA and PVDF-TRFE, in graph (a), and by PVP and PVDF-TRFE, in graph (b). Contrarily from the bilayer composite electrospun membranes which presented a greater V_{oc} value, these membranes had a value of 0 V since there is no upwards peak. The bilayer composite films have a polymer sheet between the electrode contact and the top film layer, which can work as an isolator justifying the 0 V value.

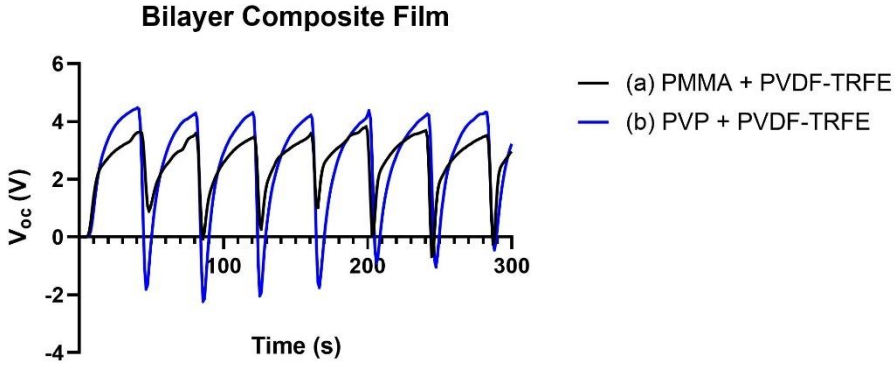

Figure 3.24 — Comparison of bilayer composite films of (a) PMMA paired with PVDF-TRFE; (b) PVP paired with PVDF-TRFE.

3.4.4 Open circuit potential - Comparative analysis

In this sub-section, the electrospun membranes are compared with the films, as well as the bi-layer composite electrospun membranes and the bilayer composite films. Three pairs of polymers are displayed in Figure 3.25, in which PVDF -TRFE was paired with PMMA, PVP and PVP.

Regarding the PMMA and PVDF-TRFE pair, the electrospun membranes provided a value of open circuit potential of 6.81 V while the films show a value of 6.63 V. These two membranes demonstrate a short difference compared to the PS and PVDF-TRFE pair which displayed a V_{oc} value of 7.12

V for the electrospun membrane and 6.54 V in the film pair. Lastly, a bigger difference was given by the PVP and PVDF-TRFE pair, that the value for the electrospun membranes is 7.31 V and the for the films is 5.22 V.

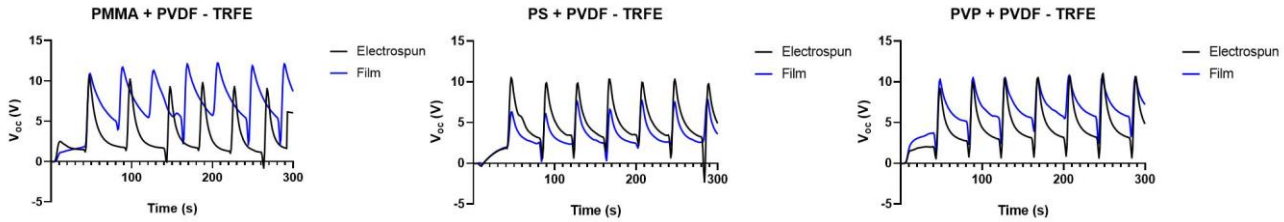

Figure 3.25 — Comparison between electrospun membranes and films.

In conclusion, the electrospun membranes provided a more substantial value of open circuit potential being more suitable than the films for the TENG application. This increased value of V_{oc} can be justified by the increased surface area provided by the electrospun membranes. The employed electrospun membranes provided an increase of 2.7%, 8.9% and 40%, respectively for pairs of PMMA, PS and PVP. These results prove once again, similar to literature, that electrospun membranes have enhanced output performance [80].

In Figure 3.26 the bilayer composite electrospun membranes are compared with the bilayer composite films, using a pair of PMMA and PVDF-TRFE and another pair of PVP and PVDF-TRFE membranes.

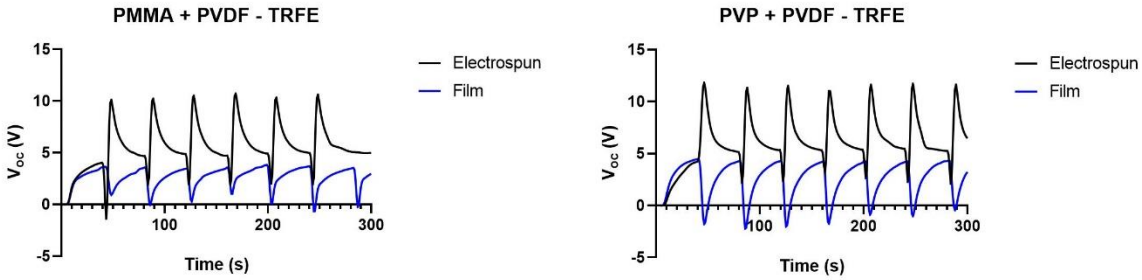

Figure 3.26 — Comparison between bilayer composite electrospun membranes and bilayer composite films.

Since both pairs of bilayer composite films provide an open circuit potential value of 0 V, the best membranes are electrospun membranes. The displayed values for the PMMA paired with PVDF-TRFE and PVP paired with PVDF-TRFE bilayer composite electrospun membranes are 5.80 V and 6.50 V, respectively. In literature there is no evidence of bilayer composite electrospun membranes, making this topic, consequently, hard to refute. In conclusion, this topic requires further investigation to compare the performance of single layer electrospun membranes and bilayer composite electrospun membranes.

3.4.5 Short circuit current - System behavior and data analysis

This sub-section is dedicated to the means of understanding the system behavior and data analysis for the short circuit current. The I_{sc} was measured with a potentiostat in the chronoamperometry mode with a voltage of 0 V. In Figure 3.27 is displayed the obtained data relative to a pair of electrospun membranes composed by PMMA and PVDF-TRFE. The mechanism used was the gravitational triboelectricity mechanism in which for trial (a) the working membrane was dropped, making one

contact in every 20 seconds, for trial (b) there was no contact and for trial (c) multiple contacts were made in periods of 20 seconds.

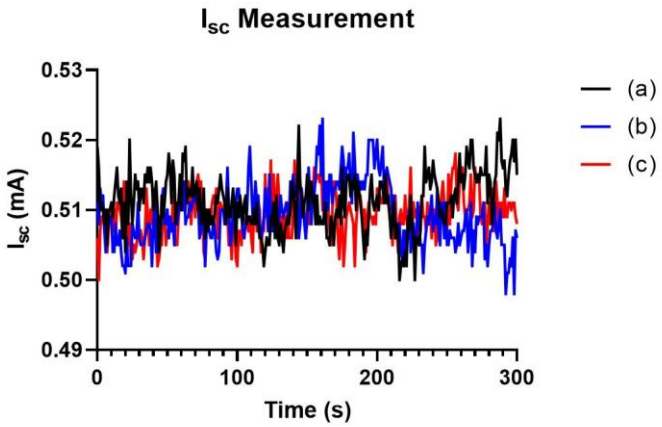

Figure 3.27 — I_{sc} measurement of electrospun PMMA paired PVDF-TRFE with (a) one contact every 20 seconds; (b) no contacts and (c) multiple contacts.

Regarding the obtained results, all the data showed a constant value of short circuit current without great variation, independently having contacts. In literature, to measure the short circuit current, chronoamperometry has been used, providing a I_{sc} graph with variation peak, variable with the contact [81]. However, this constant value can be justified by the Steady-State Operation because since the voltage is held constant at 0 V the TENG is operating in a steady-state condition where the electrical current is stable [82].

In conclusion, despite having contacts the short circuit current value for this pair of membranes is the same without contacts. The PMMA and PVDF-TRFE pair displayed values of 0.511 mA, 0.509 mA and 0.509 mA, for trials (a), (b) and (c), respectively. In literature, is not common evidence of short circuit current graphs without variation on contact. However, all the acquired I_{sc} data in this work is 10 times greater than the presented data in literature [83]–[85]. In the next sub-sections, the displayed graphs of the acquired data were with steady membranes, with no contacts.

3.4.6 Short circuit current - Electrospun membranes

In this sub-section, the short circuit current of the randomly orientated electrospun membranes can be observed. Similar to the open circuit potential section, the electrospun membranes were tested with the intention of being compared. Cellulose Acetate was used in the short circuit current tests, as reference and counter membrane with PVDF-TRFE, PVDF, HPC and PCL, and as working membrane with PMMA, PVA, PS and PVP.

In Figure A.21 (Available in Annex A.9) the CA paired with PVDF-TRFE, PVDF, PCL and HPC provides values of short circuit current of 0.497 mA, 0.540 mA, 0.555 mA, and 0.552 mA, respectively. The pairs of CA with PVA, PMMA, PS and PVP display the values 0.549 mA, 0.494 mA, 0.491 mA and 0.548 mA, respectively.

For the purpose of making a distinction between single layer and bilayer composite electrospun membranes, Figure 3.28 is displayed. In this figure are exhibited two graphs, one for a pair of PMMA and PVDF-TRFE and another for a pair of PVP and PVDF-TRFE. In each graph the trial (a) stands for single layer electrospun membranes and trial (b) for bilayer composite electrospun membranes.

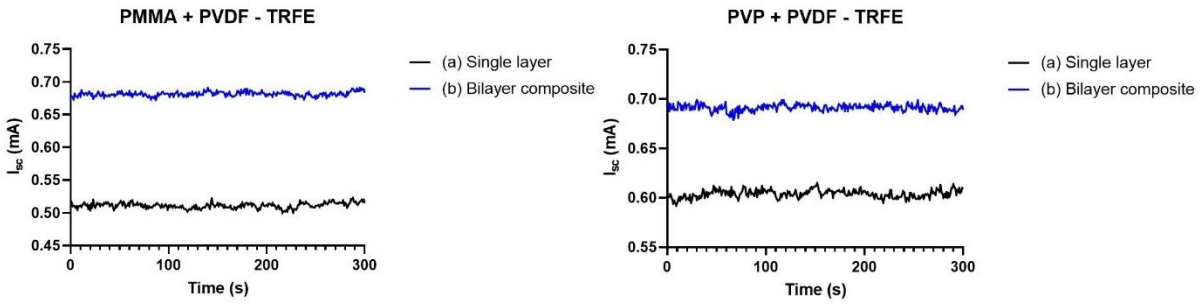

Figure 3.28 — Comparison of (a) single layer electrospun membranes and (b) bilayer composite electrospun membranes of PVDF-TRFE paired with PMMA and PVP.

The PMMA paired with PVDF-TRFE provided a short circuit current value of 0.511 mA for the single layer membranes and 0.681 mA for the bilayer composite electrospun membranes. In the case of the pair of PVP and PVDF-TRFE, the I_{sc} value is 0.604 mA and 0.691 mA, for single layer and bilayer composite electrospun membranes, respectively.

3.4.7 Short circuit current - Films

In this section, the short circuit current of the films is analyzed. To understand if the membrane thickness has an impact on the film's short circuit current, membranes with 50 µm and 200 µm are shown in Figure 3.29. This figure displays the data for a pair of PMMA and PVDF-TRFE membranes and another of PS paired with PVDF-TRFE.

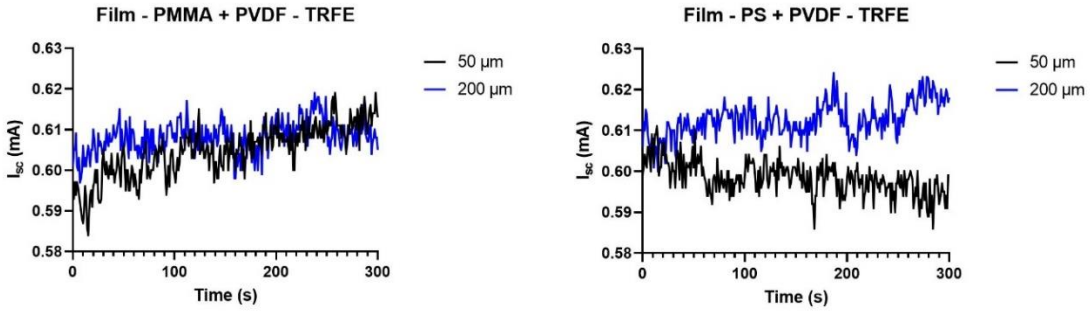

Figure 3.29 — Short circuit current of 50 µm and 200 µm thickness in films of PMMA and PS paired with PVDF-TRFE.

For the PMMA and PVDF-TRFE graph, the I_{sc} value is 0.605 mA and 0.608 mA, for 50 µm and 200 µm, respectively. In the case of the PS and PVDF-TRFE graph, the short circuit current value is 0.598 mA and 0.613 mA, for 50 µm and 200 µm, respectively. Once again, the substantially greater thickness has no relevant impact on the short circuit current values and the current generation is a surface phenomenon.

The films were also randomly paired for the short circuit current tests. In Figure A.22 (Available in Annex A.10) the pairs and the data regarding the I_{sc} trials are displayed. The obtained short circuit current for the PVP and PVDF-TRFE, PVA and PVDF-TRFE, PVA and CA, PMMA and HPC, and, PS and PVDF film pairs are 0.688 mA, 0.687 mA, 0.691 mA, 0.684 mA and 0.709 mA, respectively. These values, despite being greater than the previous films, their variation is not significant.

In Figure 3.30 the short circuit current values acquired for bilayer composite films are compared with the data regarding single layer films. In this figure, the polymers used are PMMA paired with PVDF-TRFE and PVP paired with PVDF-TRFE, in (a) as single layer films and in (b) bilayer composite films.

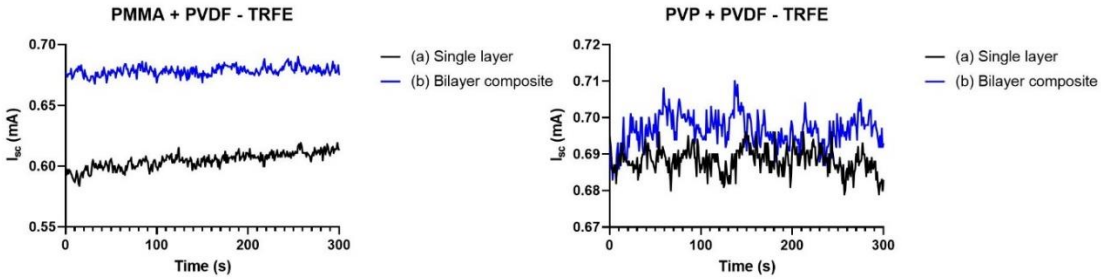

Figure 3.30 — Comparison of (a) single layer films and (b) bilayer composite films of PVDF-TRFE paired with PMMA and PVP.

For the PMMA and PVDF-TRFE pair the short circuit current values are 0.605 mA and 0.678 mA, respectively for trials (a) and (b). In the case of the PVP and PVDF-TRFE pair, the acquired values are 0.688 mA for the single layer films and 0.697 mA for the bilayer composite films. Despite the PVP and PVDF-TRFE pair having a lower value contrast between single layer and bilayer composite films, the bilayer composite films provide a greater value of short circuit current. By adding a second polymer layer the short circuit increased 12.1% and 1.3%, respectively.

3.4.8 Short circuit current - Comparative analysis

This sub-section is dedicated to compare the electrical performance of electrospun and films. In Figure 3.31 is displayed the acquired data regarding the single layer and bilayer composite electrospun and films for the PMMA and PVDF-TRFE pairs as well as for PVP and PVDF-TRFE pairs.

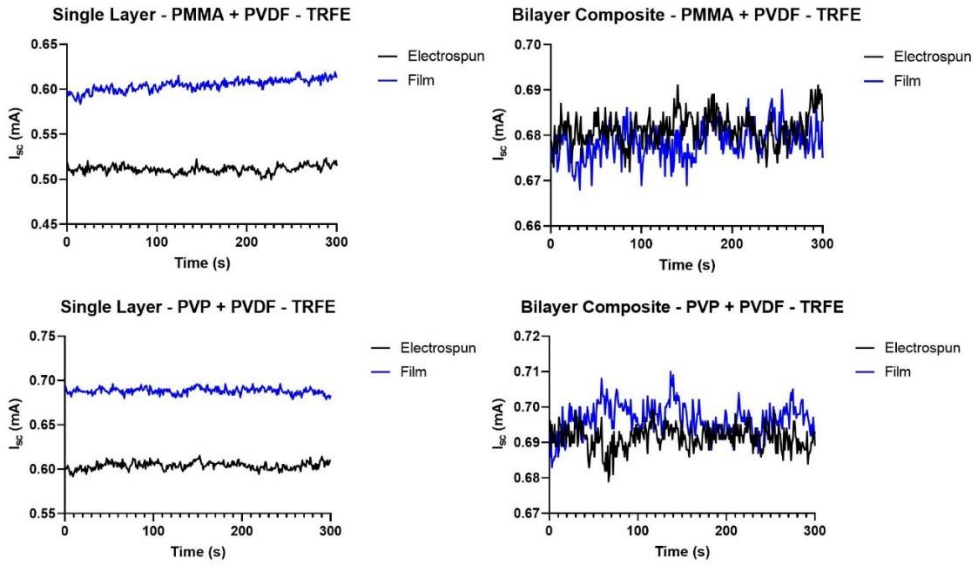

Figure 3.31 — Comparative performance analysis of electrospun and films

Regarding the single-layer membranes, both polymer pairs provided a greater short circuit current value for the films. The PMMA and PVDF-TRFE pair provided a I_{sc} value of 0.511 mA and 0.605 mA for electrospun and films, respectively. The PVP and PVDF-TRFE pair provided a short circuit current value of 0.604 mA and 0.688 mA for electrospun and films, respectively.

Concerning the bilayer composite membranes, the displayed short circuit current value is similar for both electrospun membranes and films, as well, greater than the value obtained in the single layer membranes. The PMMA and PVDF-TRFE pair provided a I_{sc} value of 0.681 mA and 0.678 mA for electrospun and films, respectively. The PVP and PVDF-TRFE pair provided a short circuit current value of 0.691 mA and 0.697 mA for electrospun and films, respectively.

All the obtained values for the open circuit voltage and the short circuit current measurements are displayed in table 3.2.

Table 3.2 – Obtained values of open circuit voltage and short circuit current for the polymeric pairs of randomly aligned electrospun membranes, polymer films, bilayer composite electrospun membranes and bilayer composite films.

Polymeric Pairs	**V_{oc} (V) / I_{sc} (mA)**			
	Electrospun Membranes	**Polymer Films**	**Bilayer Composite Electrospun Membranes**	**Bilayer Composite Films**
CA / HPC	0.787 V / 0.552 mA	-	-	-
CA / PCL	0.792 V / 0.555 mA	-	-	-
CA / PVDF	5.96 V / 0.540 mA	-	-	-
CA / PVDF-TRFE	6.84 V / 0.497 mA	-	-	-
PVA / CA	0.85 V / 0.497 mA	1.20 V	-	-
PMMA / CA	3.33 V / 0.494 mA	-	-	-
PS / CA	6.29 V / 0.491 mA	-	-	-
PVP / PVP	6.35 V / 0.548 mA	-	-	-
PMMA / HPC	-	Inconclusive	-	-
PS / PVDF	-	4.55 V	-	-
PMMA / PVDF-TRFE	6.81 V / 0.511 mA	6.63 V / 0.605 mA	5.80 V / 0.681 mA	0 V / 0.678 mA
PS / PVDF-TRFE	7.12 V	6.54 V	-	-
PVP / PVDF-TRFE	7.31 V / 0.604 mA	5.22 V / 0.688 mA	6.50 V / 0.691 mA	0 V / 0.697 mA

4
CONCLUSIONS

In this work, a comprehensive study was executed on the exploration of electrospun membranes for triboelectric applications. The investigation required electrospun membranes, films, and their respective bilayer composite membranes, produced from nine different polymeric solutions. The chosen and tested polymers were PVDF-TRFE, PVDF, PCL, HPC, CA, PVA, PMMA, PS and PVP. These polymers were selected to verify the impact of the greater surface area of the electrospun membranes and the expected increase in the electrical performance. The mechanical properties of randomly aligned electrospun membranes were studied via tensile testing. Some 3D printed objects were developed and employed for the electrochemical characterization and study of the triboelectric mechanisms for all the produced membranes. Furthermore, the randomly aligned electrospun membranes were observed for their chemical and morphology properties. Fourier-transform infrared spectroscopy (FTIR) was used for chemical characterization, and scanning electron microscopy (SEM) for surface morphology analysis. The insights of this research exhibit important data, revealing significant information for both the scientific community and practical TENG applications.

The SEM analysis of the electrospun membranes revealed some clear images regarding the surface morphology. All polymers provided a clear image of the membrane's fibers, with the exception of HPC and PVP. In these membranes, the fibers are not visible, instead, they are melted. The FTIR data helped understand the existence of excess solvent in the membranes. For the HPC membranes could be a result of having a solution with a low concentration and non-optimized electrospinning conditions. Moreover, both PVP and HPC membranes used organic solvents which are soluble in water, so the melting fibers could also be a consequence of incorrect crosslinking parameters for the PVP membranes and not performed crosslinking for the HPC membranes. Concerning the other membranes, a clear image was obtained which allowed the measuring of the average fiber diameter. The membrane with the biggest fiber diameter was PS with 3.379 ± 0.184 μm and the membrane with the smallest fibers was PVA with 0.511 ± 0.324 μm. Also, being PVDF-TRFE an important polymer in this work, the respective fiber diameter is 0.786 ± 0.317 μm. To conclude on this topic, the fiber diameter was shown to have no impact on the mechanical and electrochemical properties.

Employing FTIR analysis, the chemical composition of the electrospun membranes was studied. This approach allowed the identification of characteristic peaks corresponding to specific functional groups within the membranes. This data analysis allowed the verification of the compounds used in the membrane production, as well as their properties. Furthermore, with the support of FTIR was possible to identify the excess of some solvents and later back up the SEM analysis.

Regarding the mechanical characterization of the randomly aligned electrospun membranes, their data revealed different outcomes for each membrane. In terms of strain, PVDF-TRFE and PCL were the most dominant membranes, providing an elongation in percentage of 297 ± 37 and 219 ± 4, respectively. Relatively to the ultimate tensile strength, PVDF-TRFE was again the polymer which presented the greater value, reaching 11.75 ± 0.91 MPa. Concerning the Young's modulus, the top polymeric electrospun membranes were made with PVP, CA and PVA displaying the values 72.34 ± 7.22 MPa, 69.76 ± 10.95 MPa and 63.25 ± 13.27 MPa. PVP was the membrane that held the greater stress for the same amount of strain. This value revelation implies that these polymers provide significant capability for TENG applications. PVDF-TRFE, due to its high strain and ultimate tensile strength, provide the ability to be used as flexible and wearable TENGs, being one of the best polymers. Moreover, in terms of Young's modulus, PVP exhibited a greater value, being also relevant for the TENG applications. This polymer and the others with a higher Young's modulus have the ability to withstand

higher elastic deformations and being stiffer show great use in vertical contact mode for triboelectric applications.

To conclude on the electrochemical characterization, the randomly aligned, films and respective bilayer composite membranes were analyzed. The used mechanisms were the vertical contact and lateral sliding modes. The characterization began with the jigsaw and rotational triboelectricity using a multimeter, but the data was difficult to measure, the results were uncertain and the membranes experienced a substantial grade of tear and wear. Later, the manual triboelectricity method was implemented, but once again, the same measuring problems were observed. The final results were obtained using the gravitational triboelectricity method, which exhibited constant and real values of the measured open circuit potential and short circuit current.

Regarding the V_{oc} measurements, it was possible to assemble a triboelectric series for the nine polymers. From the material with the highest to the lowest potential, the series is constituted by PVDF-TRFE, PVDF, PCL, HPC, CA, PVA, PMMA, PS and PVP. The pairs which provided the highest values of V_{oc} were PVDF-TRFE paired with PMMA, PS and PVP. The comparison between electrospun and films was made for these pairs. The electrospun membranes displayed an open circuit potential increase of 2.7%, 8.9% and 40%, respectively for the pairs with PMMA, PS and PVP. Is possible to conclude that the electrospun membranes provided a greater value of open circuit potential than the films, confirming the increased performance from the larger surface area of the electrospun membranes. The bilayer composite films of PMMA paired with PVDF-TRFE and PVP paired with PVDF-TRFE presented a V_{oc} value of 0 V, which is a positive outcome for the bilayer composite electrospun membranes displaying 5.80 V and 6.50 V, respectively.

Regarding the I_{sc} measurements, the obtained values displayed a I_{sc} graph without variation peaks. This constant value was justified by the Steady-State Operation in which the electrical current was stable. In order to distinguish the film from the electrospun membranes, PVDF-TRFE was paired with PMMA and with PVP. The films provided a bigger value, 0.605 mA and 0.688 mA, than the electrospun membranes, 0.511 mA and 0.604 mA, respectively. Concerning the bilayer composite membranes, they displayed a greater short circuit value than the single layer membranes. Furthermore, both bilayer composite film and electrospun membranes acquired a similar I_{sc} value, being in the PMMA and PVDF-TRFE pair 0.681 mA and 0.678 mA, and in the PVP and PVDF-TRFE pair 0.691 mA and 0.697 mA, respectively.

However, it is important to understand the limitations of this study. Further research could examine other factors that influence the membrane's properties and parameters. Regarding material selection, different materials could be selected and paired into different combinations to enhance electrochemical properties. Instead of randomly aligned fibers, the electrospinning of membranes with aligned fibers could be also studied for the improvement of mechanical and electrochemical properties. More on the electrospinning, the conditions relative to HPC and PVP should be reviewed to avoid melted fibers. Different triboelectric mechanisms could also be investigated like the lateral sliding mode with the objective of quantifying and reducing the membrane's wear and tear. Lastly, the bilayer composite electrospun membranes revealed to be an interesting membrane variation, exhibiting good values of V_{oc} and I_{sc}, however it needs further attention. Long-term studies should explore the stability and performance of these membranes for practical applications and real-world solutions.

In conclusion, this work provides new information on the study of electrospun membranes, films, and bilayer composite membranes. By conducting mechanical, structural, and chemical analyses, this work has provided a comprehensive view of these polymers and their potential. The pair that exhibited the best performance in both single layer and bilayer membranes was composed by PVDF-TRFE and PVP adding also their suitable mechanical properties. Furthermore, the bilayer composite electrospun membranes despite having a lower V_{oc}, overall, provided better results than the single layer films and membranes. As we walk towards a period of energy crisis and high demands, innovative and sustainable materials are required. This research supports a foundation for future improvements in membrane technology.

REFERENCES

[1] J. M. Lourenço, "The NOVAthesis LATEX Template User's Manual," NOVA University, Lisbon, 2021. Accessed: Oct. 03, 2023. [Online]. Available: https://github.com/joaomlourenco/novathesis_word/raw/master/novathesis_word-FINAL-EN.pdf

[2] Q. Abu Al-Haija, "A Stochastic Estimation Framework for Yearly Evolution of Worldwide Electricity Consumption," *Forecasting*, vol. 3, no. 2, pp. 256–266, Apr. 2021, doi: 10.3390/forecast3020016.

[3] S. Thomas and J. Rosenow, "Drivers of increasing energy consumption in Europe and policy implications," *Energy Policy*, vol. 137, p. 111108, Feb. 2020, doi: 10.1016/j.enpol.2019.111108.

[4] M. Azam, L. Liu, and N. Ahmad, "Impact of institutional quality on environment and energy consumption: evidence from developing world," *Environ Dev Sustain*, vol. 23, no. 2, pp. 1646–1667, Feb. 2021, doi: 10.1007/s10668-020-00644-x.

[5] S. Shafiee and E. Topal, "When will fossil fuel reserves be diminished?," *Energy Policy*, vol. 37, no. 1, pp. 181–189, Jan. 2009, doi: 10.1016/j.enpol.2008.08.016.

[6] REN21, "Renewables 2023 Global Status Report Collection," Paris, 2023. Accessed: Aug. 16, 2023. [Online]. Available: https://www.ren21.net/wp-content/uploads/2019/05/GSR2023_GlobalOverview_Full_Report_with_endnotes_web.pdf

[7] Mark P. Mills, "Mines, Minerals, and 'Green' Energy: A Reality Check," Jul. 2020. Accessed: Aug. 15, 2023. [Online]. Available: http://www.goinggreencanada.ca/green_energy_reality_check.pdf

[8] R. Kothari, V. V. Tyagi, and A. Pathak, "Waste-to-energy: A way from renewable energy sources to sustainable development," *Renewable and Sustainable Energy Reviews*, vol. 14, no. 9, pp. 3164–3170, Dec. 2010, doi: 10.1016/j.rser.2010.05.005.

[9] J. Mohtasham, "Review Article-Renewable Energies," *Energy Procedia*, vol. 74, pp. 1289–1297, Aug. 2015, doi: 10.1016/j.egypro.2015.07.774.

[10] Z. Lin, J. Chen, and J. Yang, "Recent Progress in Triboelectric Nanogenerators as a Renewable and Sustainable Power Source," *J Nanomater*, vol. 2016, pp. 1–24, 2016, doi: 10.1155/2016/5651613.

[11] Z. L. Wang, "Triboelectric Nanogenerators as New Energy Technology for Self-Powered Systems and as Active Mechanical and Chemical Sensors," *ACS Nano*, vol. 7, no. 11, pp. 9533–9557, Nov. 2013, doi: 10.1021/nn404614z.

[12] Y. Li *et al.*, "Advances in electrospun nanofibers for triboelectric nanogenerators," *Nano Energy*, vol. 104, p. 107884, Dec. 2022, doi: 10.1016/j.nanoen.2022.107884.

[13] T. Cheng, Q. Gao, and Z. L. Wang, "The Current Development and Future Outlook of Triboelectric Nanogenerators: A Survey of Literature," *Adv Mater Technol*, vol. 4, no. 3, p. 1800588, Mar. 2019, doi: 10.1002/admt.201800588.

[14] Y. Li *et al.*, “Advances in electrospun nanofibers for triboelectric nanogenerators,” *Nano Energy*, vol. 104, p. 107884, Dec. 2022, doi: 10.1016/j.nanoen.2022.107884.

[15] G. Zhu, B. Peng, J. Chen, Q. Jing, and Z. Lin Wang, “Triboelectric nanogenerators as a new energy technology: From fundamentals, devices, to applications,” *Nano Energy*, vol. 14, pp. 126–138, May 2015, doi: 10.1016/j.nanoen.2014.11.050.

[16] Q. Liu, J. Zhu, L. Zhang, and Y. Qiu, “Recent advances in energy materials by electrospinning,” *Renewable and Sustainable Energy Reviews*, vol. 81, pp. 1825–1858, Jan. 2018, doi: 10.1016/j.rser.2017.05.281.

[17] Y. Kim, X. Wu, and J. H. Oh, “Fabrication of triboelectric nanogenerators based on electrospun polyimide nanofibers membrane,” *Sci Rep*, vol. 10, no. 1, p. 2742, Feb. 2020, doi: 10.1038/s41598-020-59546-7.

[18] A. Babu, I. Aazem, R. Walden, S. Bairagi, D. M. Mulvihill, and S. C. Pillai, “Electrospun nanofiber based TENGs for wearable electronics and self-powered sensing,” *Chemical Engineering Journal*, vol. 452, p. 139060, Jan. 2023, doi: 10.1016/j.cej.2022.139060.

[19] C. Luo *et al.*, “Preparation and application of high performance PVDF/PS electrospinning film-based triboelectric nanogenerator,” *Chem Phys Lett*, vol. 813, p. 140276, Feb. 2023, doi: 10.1016/j.cplett.2022.140276.

[20] C. Garcia, I. Trendafilova, R. Guzman de Villoria, and J. Sanchez del Rio, “Self-powered pressure sensor based on the triboelectric effect and its analysis using dynamic mechanical analysis,” *Nano Energy*, vol. 50, pp. 401–409, Aug. 2018, doi: 10.1016/j.nanoen.2018.05.046.

[21] Y. Bai, Z. Zhou, Q. Zhu, S. Lu, Y. Li, and L. Ionov, “Electrospun cellulose acetate nanofibrous composites for multi-responsive shape memory actuators and self-powered pressure sensors,” *Carbohydr Polym*, vol. 313, p. 120868, Aug. 2023, doi: 10.1016/j.carbpol.2023.120868.

[22] H. G. Menge, N. D. Huynh, H. J. Hwang, S. Han, D. Choi, and Y. T. Park, “Designable Skin-like Triboelectric Nanogenerators Using Layer-by-Layer Self-Assembled Polymeric Nanocomposites,” *ACS Energy Lett*, vol. 6, no. 7, pp. 2451–2459, Jul. 2021, doi: 10.1021/acsenergylett.1c00739.

[23] Z. Niu *et al.*, “Recent advances in cellulose-based flexible triboelectric nanogenerators,” *Nano Energy*, vol. 87, p. 106175, Sep. 2021, doi: 10.1016/j.nanoen.2021.106175.

[24] X. Wang, C. Yao, F. Wang, and Z. Li, “Cellulose-Based Nanomaterials for Energy Applications,” *Small*, vol. 13, no. 42, Nov. 2017, doi: 10.1002/smll.201702240.

[25] C. Yao, X. Yin, Y. Yu, Z. Cai, and X. Wang, “Chemically Functionalized Natural Cellulose Materials for Effective Triboelectric Nanogenerator Development,” *Adv Funct Mater*, vol. 27, no. 30, p. 1700794, Aug. 2017, doi: 10.1002/adfm.201700794.

[26] N. Wang *et al.*, “Anisotropic Triboelectric Nanogenerator Based on Ordered Electrospinning,” *ACS Appl Mater Interfaces*, vol. 12, no. 41, pp. 46205–46211, Oct. 2020, doi: 10.1021/acsami.0c13938.

[27] Z. L. Wang, “Triboelectric nanogenerators as new energy technology for self-powered systems and as active mechanical and chemical sensors.,” *ACS Nano*, vol. 7, no. 11, pp. 9533–57, Nov. 2013, doi: 10.1021/nn404614z.

[28] J. Luo and Z. L. Wang, “Recent progress of triboelectric nanogenerators: From fundamental theory to practical applications,” *EcoMat*, vol. 2, no. 4, Dec. 2020, doi: 10.1002/eom2.12059.

[29] F. Yi, Z. Zhang, Z. Kang, Q. Liao, and Y. Zhang, “Recent Advances in Triboelectric Nanogenerator-Based Health Monitoring,” *Adv Funct Mater*, vol. 29, no. 41, Oct. 2019, doi: 10.1002/adfm.201808849.

[30] Z. L. Wang, “Triboelectric Nanogenerator (TENG)—Sparking an Energy and Sensor Revolution,” *Adv Energy Mater*, vol. 10, no. 17, May 2020, doi: 10.1002/aenm.202000137.

[31] H. Zhang, Y. Yang, T.-C. Hou, Y. Su, C. Hu, and Z. L. Wang, “Triboelectric nanogenerator built inside clothes for self-powered glucose biosensors,” *Nano Energy*, vol. 2, no. 5, pp. 1019–1024, Sep. 2013, doi: 10.1016/j.nanoen.2013.03.024.

[32] R. Zhang *et al.*, “The triboelectricity of the human body,” *Nano Energy*, vol. 86, p. 106041, Aug. 2021, doi: 10.1016/j.nanoen.2021.106041.

[33] S. Liu, T. Hua, X. Luo, N. Yi Lam, X. Tao, and L. Li, “A novel approach to improving the quality of chitosan blended yarns using static theory,” *Textile Research Journal*, vol. 85, no. 10, pp. 1022–1034, Jun. 2015, doi: 10.1177/0040517514559576.

[34] K. Venugopal, P. Panchatcharam, A. Chandrasekhar, and V. Shanmugasundaram, “Comprehensive Review on Triboelectric Nanogenerator Based Wrist Pulse Measurement: Sensor Fabrication and Diagnosis of Arterial Pressure,” *ACS Sens*, vol. 6, no. 5, pp. 1681–1694, May 2021, doi: 10.1021/acssensors.0c02324.

[35] C. Wu, A. C. Wang, W. Ding, H. Guo, and Z. L. Wang, “Triboelectric Nanogenerator: A Foundation of the Energy for the New Era,” *Adv Energy Mater*, vol. 9, no. 1, p. 1802906, Jan. 2019, doi: 10.1002/aenm.201802906.

[36] T. Jirabovornwisut and A. Arpornwichanop, “A review on the electrolyte imbalance in vanadium redox flow batteries,” *Int J Hydrogen Energy*, vol. 44, no. 45, pp. 24485–24509, Sep. 2019, doi: 10.1016/j.ijhydene.2019.07.106.

[37] P. Kurzweil, “BATTERIES | Nomenclature,” in *Encyclopedia of Electrochemical Power Sources*, Elsevier, 2009, pp. 381–394. doi: 10.1016/B978-044452745-5.00042-3.

[38] F. E. Ahmed, B. S. Lalia, and R. Hashaikeh, “A review on electrospinning for membrane fabrication: Challenges and applications,” *Desalination*, vol. 356, pp. 15–30, Jan. 2015, doi: 10.1016/j.desal.2014.09.033.

[39] A. Balguild, A. Mol, M. H. van Marion, R. A. Bank, C. V.C. Bouten, and F. P.T. Baaijens, “Tissue Engineering: Part A,” 2009. doi: 10.1089=ten.tea.2007.0294.

[40] S. Wilk and A. Benko, “Advances in Fabricating the Electrospun Biopolymer-Based Biomaterials,” *J Funct Biomater*, vol. 12, no. 2, p. 26, Apr. 2021, doi: 10.3390/jfb12020026.

[41] F. E. Ahmed, B. S. Lalia, and R. Hashaikeh, “A review on electrospinning for membrane fabrication: Challenges and applications,” *Desalination*, vol. 356, pp. 15–30, Jan. 2015, doi: 10.1016/j.desal.2014.09.033.

[42] D. R. Nisbet, A. E. Rodda, D. I. Finkelstein, M. K. Horne, J. S. Forsythe, and W. Shen, “Surface and bulk characterisation of electrospun membranes: Problems and improve-

ments," *Colloids Surf B Biointerfaces*, vol. 71, no. 1, pp. 1–12, Jun. 2009, doi: 10.1016/j.colsurfb.2009.01.022.

[43] J. R. Davis, *Tensile Testing*, 2nd Edition. Ohio, 2004. Accessed: Aug. 29, 2023. [Online]. Available: https://books.google.pt/books?id=5uRlb3emLY8C&dq=tensile+tests&lr=&hl=pt-PT&source=gbs_navlinks_s

[44] A. P. C. Almeida, J. Oliveira, S. N. Fernandes, M. H. Godinho, and J. P. Canejo, "All-cellulose composite membranes for oil microdroplet collection," *Cellulose*, vol. 27, no. 8, pp. 4665–4677, May 2020, doi: 10.1007/s10570-020-03077-x.

[45] E. T. Suryandari, M. A. Zulfikar, R. R. Mukti, and M. Nasir, "Preparation and Characterization of Poly(Methyl Methacrylate) (PMMA) Fibers by Electrospinning," *Key Eng Mater*, vol. 811, pp. 163–169, Jul. 2019, doi: 10.4028/www.scientific.net/KEM.811.163.

[46] A. Gonçalves *et al.*, "Engineering dual-stimuli responsive poly(vinyl alcohol) nanofibrous membranes for cancer treatment by magnetic hyperthermia," *Biomaterials Advances*, vol. 145, p. 213275, Feb. 2023, doi: 10.1016/j.bioadv.2022.213275.

[47] M. T. Hasan, R. Gonzalez, A. A. Munoz, L. Materon, J. G. Parsons, and M. Alcoutlabi, "Forcespun polyvinylpyrrolidone/copper and polyethylene oxide/copper composite fibers and their use as antibacterial agents," *J Appl Polym Sci*, vol. 139, no. 11, Mar. 2022, doi: 10.1002/app.51773.

[48] S. Shukla, E. Brinley, H. J. Cho, and S. Seal, "Electrospinning of hydroxypropyl cellulose fibers and their application in synthesis of nano and submicron tin oxide fibers," *Polymer (Guildf)*, vol. 46, no. 26, pp. 12130–12145, Dec. 2005, doi: 10.1016/j.polymer.2005.10.070.

[49] T. Uyar and F. Besenbacher, "Electrospinning of uniform polystyrene fibers: The effect of solvent conductivity," *Polymer (Guildf)*, vol. 49, no. 24, pp. 5336–5343, Nov. 2008, doi: 10.1016/j.polymer.2008.09.025.

[50] A. Cipitria, A. Skelton, T. R. Dargaville, P. D. Dalton, and D. W. Hutmacher, "Design, fabrication and characterization of PCL electrospun scaffolds—a review," *J Mater Chem*, vol. 21, no. 26, p. 9419, 2011, doi: 10.1039/c0jm04502k.

[51] S. Saha, V. Yauvana, S. Chakraborty, and D. Sanyal, "Synthesis and Characterization of Polyvinylidene-fluoride (PVDF) Nanofiber for Application as Piezoelectric Force Sensor," *Mater Today Proc*, vol. 18, pp. 1450–1458, 2019, doi: 10.1016/j.matpr.2019.06.613.

[52] L. T. Beringer, X. Xu, W. Shih, W. H. Shih, R. Habas, and C. L. Schauer, "An electrospun PVDF-TrFe fiber sensor platform for biological applications," *Sens Actuators A Phys*, vol. 222, pp. 293–300, Feb. 2015, doi: 10.1016/j.sna.2014.11.012.

[53] J. Lin, B. Ding, and J. Yu, "Direct Fabrication of Highly Nanoporous Polystyrene Fibers via Electrospinning," *ACS Appl Mater Interfaces*, vol. 2, no. 2, pp. 521–528, Feb. 2010, doi: 10.1021/am900736h.

[54] R. D. Simoes, M. A. Rodriguez-Perez, J. A. de Saja, and C. J. L. Constantino, "Thermomechanical characterization of PVDF and P(VDF-TrFE) blends containing corn starch and natural rubber," *J Therm Anal Calorim*, vol. 99, no. 2, pp. 621–629, Feb. 2010, doi: 10.1007/s10973-009-0285-z.

[55] W. E. Mahmoud and S. A. Al-Bluwi, “Development of highly sensitive temperature sensor made of graphene monolayers doped P(VDF-TrFE) nanocomposites,” *Sens Actuators A Phys*, vol. 312, p. 112101, Sep. 2020, doi: 10.1016/j.sna.2020.112101.

[56] E. Benedetti *et al.*, “FTIR-Microspectroscopy andDSC Studies of Poly(vinylidene fluoride),” *Polym Int*, vol. 41, no. 1, pp. 35–41, Sep. 1996, doi: 10.1002/(SICI)1097-0126(199609)41:1<35::AID-PI579>3.0.CO;2-T.

[57] T. Elzein, M. Nasser-Eddine, C. Delaite, S. Bistac, and P. Dumas, “FTIR study of polycaprolactone chain organization at interfaces,” *J Colloid Interface Sci*, vol. 273, no. 2, pp. 381–387, May 2004, doi: 10.1016/j.jcis.2004.02.001.

[58] C. Zhang, Z. Ren, Z. Yin, L. Jiang, and S. Fang, “Experimental FTIR and simulation studies on H-bonds of model polyurethane in solutions. I: In dimethylformamide (DMF),” *Spectrochim Acta A Mol Biomol Spectrosc*, vol. 81, no. 1, pp. 598–603, Oct. 2011, doi: 10.1016/j.saa.2011.06.057.

[59] A. E. Wallis, J. C. Whitehead, and K. Zhang, “The removal of dichloromethane from atmospheric pressure nitrogen gas streams using plasma-assisted catalysis,” *Appl Catal B*, vol. 74, no. 1–2, pp. 111–116, Jun. 2007, doi: 10.1016/j.apcatb.2006.11.020.

[60] D. M. Verbovy, T. G. Smagala, M. A. Brynda, and W. R. Fawcett, “A FTIR study of ion-solvent interactions in N,N-dimethylacetamide,” *J Mol Liq*, vol. 129, no. 1–2, pp. 13–17, Oct. 2006, doi: 10.1016/j.molliq.2006.08.008.

[61] M. A. Hasan, M. I. Zaki, and L. Pasupulety, “Oxide-catalyzed conversion of acetic acid into acetone: an FTIR spectroscopic investigation,” *Appl Catal A Gen*, vol. 243, no. 1, pp. 81–92, Mar. 2003, doi: 10.1016/S0926-860X(02)00539-2.

[62] F. Namouchi, H. Smaoui, N. Fourati, C. Zerrouki, H. Guermazi, and J. J. Bonnet, “Investigation on electrical properties of thermally aged PMMA by combined use of FTIR and impedance spectroscopies,” *J Alloys Compd*, vol. 469, no. 1–2, pp. 197–202, Feb. 2009, doi: 10.1016/j.jallcom.2008.01.148.

[63] S.-G. Sun and Y. Lin, “Kinetics of isopropanol oxidation on Pt(111), Pt(110), Pt(100), Pt(610) and Pt(211) single crystal electrodes -,” *Electrochim Acta*, vol. 44, no. 6–7, pp. 1153–1162, Nov. 1998, doi: 10.1016/S0013-4686(98)00218-7.

[64] A. Pawlak and M. Mucha, “Thermogravimetric and FTIR studies of chitosan blends,” *Thermochim Acta*, vol. 396, no. 1–2, pp. 153–166, Feb. 2003, doi: 10.1016/S0040-6031(02)00523-3.

[65] P. Fei, L. Liao, B. Cheng, and J. Song, “Quantitative analysis of cellulose acetate with a high degree of substitution by FTIR and its application,” *Analytical Methods*, vol. 9, no. 43, pp. 6194–6201, 2017, doi: 10.1039/C7AY02165H.

[66] H. S. Mansur, R. L. Oréfice, and A. A. P. Mansur, “Characterization of poly(vinyl alcohol)/poly(ethylene glycol) hydrogels and PVA-derived hybrids by small-angle X-ray scattering and FTIR spectroscopy,” *Polymer (Guildf)*, vol. 45, no. 21, pp. 7193–7202, Sep. 2004, doi: 10.1016/j.polymer.2004.08.036.

[67] Z. H. Ping, Q. T. Nguyen, S. M. Chen, J. Q. Zhou, and Y. D. Ding, “States of water in different hydrophilic polymers — DSC and FTIR studies,” *Polymer (Guildf)*, vol. 42, no. 20, pp. 8461–8467, Sep. 2001, doi: 10.1016/S0032-3861(01)00358-5.

[68] Y. Borodko, S. E. Habas, M. Koebel, P. Yang, H. Frei, and G. A. Somorjai, “Probing the interaction of poly(vinylpyrrolidone) with platinum nanocrystals by UV - Raman and FTIR,” *Journal of Physical Chemistry B*, vol. 110, no. 46, pp. 23052–23059, Nov. 2006, doi: 10.1021/jp063338.

[69] E. L. Veale, J. Irudayaraj, and A. Demirci, “An On-Line Approach To Monitor Ethanol Fermentation Using FTIR Spectroscopy,” *Biotechnol Prog*, vol. 23, no. 2, pp. 494–500, Jan. 2007, doi: 10.1021/bp060306v.

[70] K. Sivaiah, H. Rudramadevi, S. Buddhudu, G. Bhaskar Kumar, and A. Varadarajulu, “Structural, thermal and optical properties of Cu 2+ and Co 2+ : PVP polymer films,” 2010.

[71] I. S. Elashmawi and N. A. Hakeem, “Effect of PMMA addition on characterization and morphology of PVDF,” *Polym Eng Sci*, vol. 48, no. 5, pp. 895–901, May 2008, doi: 10.1002/pen.21032.

[72] M. M. E. Jacob and A. K. Arof, “FTIR studies of DMF plasticized polyvinyledene fluoride based polymer electrolytes,” *Electrochim Acta*, vol. 45, no. 10, pp. 1701–1706, Jan. 2000, doi: 10.1016/S0013-4686(99)00316-3.

[73] L. M. M. Costa, R. E. S. Bretas, and R. Gregorio, “Effect of Solution Concentration on the Electrospray/Electrospinning Transition and on the Crystalline Phase of PVDF,” *Materials Sciences and Applications*, vol. 01, no. 04, pp. 247–252, 2010, doi: 10.4236/msa.2010.14036.

[74] A. G. Sichali, H. Noby, H. Naragino, T. Yoshitake, and A. H. El-Shazly, “Successful preparation of polyaniline-modified polystyrene novel composite membrane,” *J Appl Polym Sci*, vol. 140, no. 41, Nov. 2023, doi: 10.1002/app.54477.

[75] F. Croisier *et al.*, “Mechanical testing of electrospun PCL fibers,” *Acta Biomater*, vol. 8, no. 1, pp. 218–224, Jan. 2012, doi: 10.1016/j.actbio.2011.08.015.

[76] W. Zhang, B. Zaarour, L. Zhu, C. Huang, B. Xu, and X. Jin, “A comparative study of electrospun polyvinylidene fluoride and poly(vinylidenefluoride-co-trifluoroethylene) fiber webs: Mechanical properties, crystallinity, and piezoelectric properties,” *J Eng Fiber Fabr*, vol. 15, p. 155892502093929, Jan. 2020, doi: 10.1177/1558925020939290.

[77] S. S. Nair and A. P. Mathew, “Porous composite membranes based on cellulose acetate and cellulose nanocrystals via electrospinning and electrospraying,” *Carbohydr Polym*, vol. 175, pp. 149–157, Nov. 2017, doi: 10.1016/j.carbpol.2017.07.048.

[78] C. Narváez-Muñoz *et al.*, “Impact of the solvent composition on the structural and mechanical properties of customizable electrospun poly(vinylpyrrolidone) fiber mats,” *Physical Chemistry Chemical Physics*, vol. 23, no. 40, pp. 22923–22935, 2021, doi: 10.1039/D1CP03145G.

[79] N. Sun *et al.*, “Waterproof, breathable and washable triboelectric nanogenerator based on electrospun nanofiber films for wearable electronics,” *Nano Energy*, vol. 90, p. 106639, Dec. 2021, doi: 10.1016/j.nanoen.2021.106639.

[80] X. Ge, N. Hu, F. Yan, and Y. Wang, “Development and applications of electrospun nanofiber-based triboelectric nanogenerators,” *Nano Energy*, vol. 112, p. 108444, Jul. 2023, doi: 10.1016/j.nanoen.2023.108444.

[81] F. Ali *et al.*, “Triboelectric Nanogenerator Based on PTFE Plastic Waste Bottle and Aluminum Foil,” *Materials Innovations*, vol. 2, no. 8, pp. 203–213, Aug. 2022, doi: 10.54738/MI.2022.2803.

[82] M. Lu *et al.*, “A model for the triboelectric nanogenerator with inductive load and its energy boost potential,” *Nano Energy*, vol. 63, p. 103883, Sep. 2019, doi: 10.1016/j.nanoen.2019.103883.

[83] B. Yu, H. Yu, H. Wang, Q. Zhang, and M. Zhu, “High-power triboelectric nanogenerator prepared from electrospun mats with spongy parenchyma-like structure,” *Nano Energy*, vol. 34, pp. 69–75, Apr. 2017, doi: 10.1016/j.nanoen.2017.02.010.

[84] F. Chen *et al.*, “A novel triboelectric nanogenerator based on electrospun polyvinylidene fluoride nanofibers for effective acoustic energy harvesting and self-powered multifunctional sensing,” *Nano Energy*, vol. 56, pp. 241–251, Feb. 2019, doi: 10.1016/j.nanoen.2018.11.041.

[85] Y. Hao, J. Huang, S. Liao, D. Chen, and Q. Wei, “All-electrospun performance-enhanced triboelectric nanogenerator based on the charge-storage process,” *J Mater Sci*, vol. 57, no. 8, pp. 5334–5345, Feb. 2022, doi: 10.1007/s10853-022-06927-0.

[86] W. Liu *et al.*, “Electrospinning Assisted by Gas Jet for Preparing Ultrafine Poly (vinyl alcohol) Fibres,” 2009.

A
ANNEX

A.1 Triboelectric series

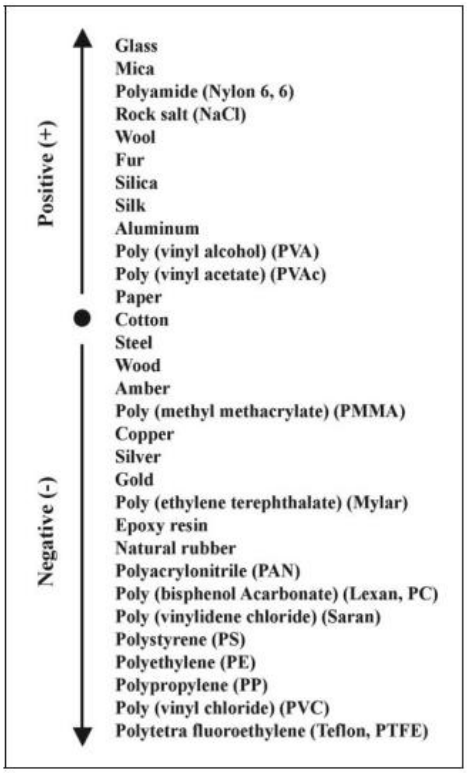

Figure A.1 — Triboelectric series for different materials [33].

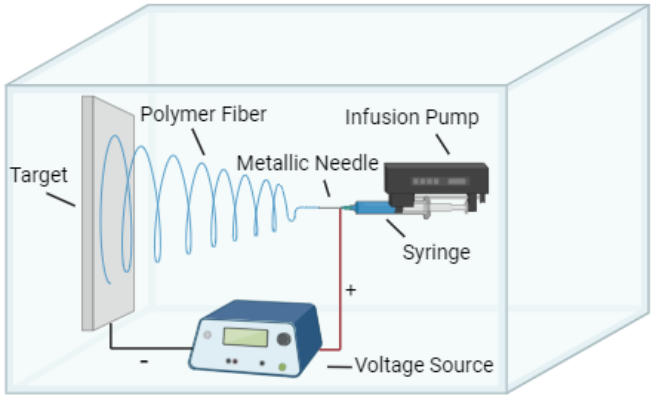

Figure A.2 — Schematic of electrospinning setup (Made with BioRender.com).

A.2 Preparation of polymeric solutions

Table A.1 — Preparation of polymeric solutions.

Polymer	Concentration	Solvents	Ratio	Agitation	Source
CA	12 wt.%	Acetone + DMAc	2:1	Magnetic, T_{amb}	[44]
PMMA	8 wt.%	DMAc + Acetone	6:4	Magnetic, T_{amb}	[45]
PVA	0.1 g/ml	Ultrapure Water	-	Mechanical, $T_{80\,°C}$	[46]
PVP	18 wt.%	EtOH	-	Magnetic, T_{amb}	[47]
HPC	15 wt.%	Isopropanol	-	Magnetic, T_{amb}	[48]
PS	0.3 g/ml	DMF	-	Magnetic, T_{amb}	[49]
PCL	13 wt.%	DCM + DMF	3:1	Magnetic, T_{amb}	[50]
PVDF	15 wt.%	1st DMF 70% (v/v), Magnetic at $T_{70\,°C}$ for 24h 2nd Acetone 30% (v/v), Magnetic at T_{amb} for 24h			[51]
PVDF-TRFE	15 wt.%	MEK + EtOH	9:1	Magnetic, T_{amb}	[52]

A.3 Electrospinning of polymeric membranes and other processes

Table A.2 — Controlled factors used in the electrospun membranes.

Polymer	Flow Rate	Voltage	Distance	Humidity	Crosslinking	Source
CA	0.2 ml/h	20 kV	15 cm	45%	No	[44]
PMMA	0.4 ml/h	20 kV	15 cm	50%	No	[45]
PVA	0.2 ml/h	20 kV	15 cm	45%	180 °C in Oven, 4h	[86]
PVP	0.14 ml/h	15kV	15 cm	45%	60 J in UV Crosslinker, 45 min	-
HPC	1.2 ml/h	20kV	15 cm	50%	No	[48]
PS	1 ml/h	15 kV	10 cm	45%	No	[49]
PCL	0.8 ml/h	15kV	15 cm	50%	No	[50]
PVDF	0.3 ml/h	20kV	10 cm	50%	No	[51]
PVDF-TRFE	0.8 ml/h	10 kV	10 cm	45%	No	[52]

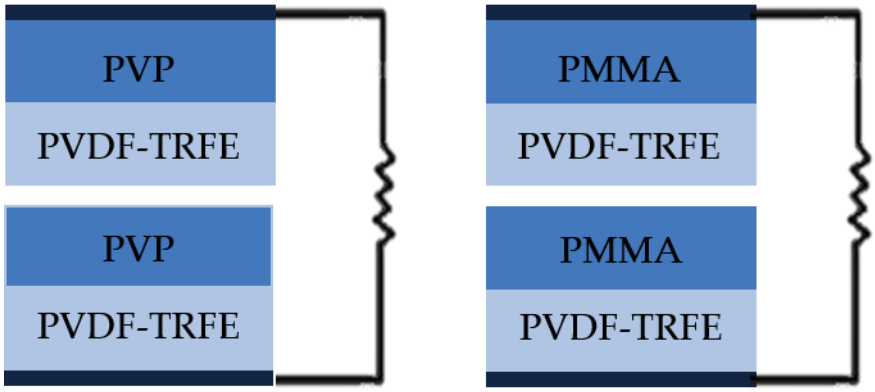

Figure A.3 — Schematic representation of the bilayer composite electrospun membranes.

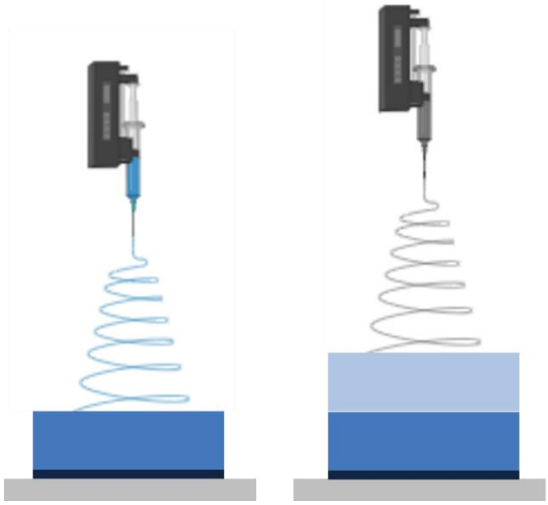

Figure A.4 — Schematic process representation of the bilayer composite electrospun membranes.

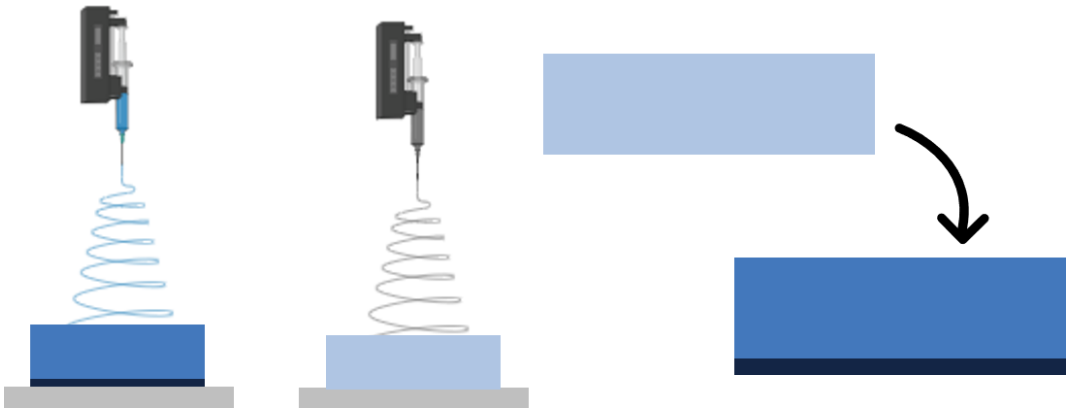

Figure A.5 — Schematic process representation of the double layer electrospun membranes.

Figure A.6 — Schematic process representation of films by casting.

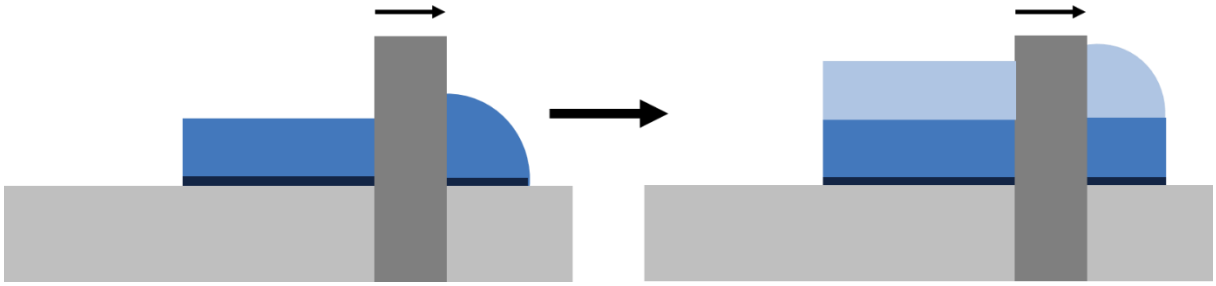

Figure A.7 — Schematic process representation of the bilayer composite films.

A.4 3D printed objects

A.4.1 Manual triboelectric mechanism

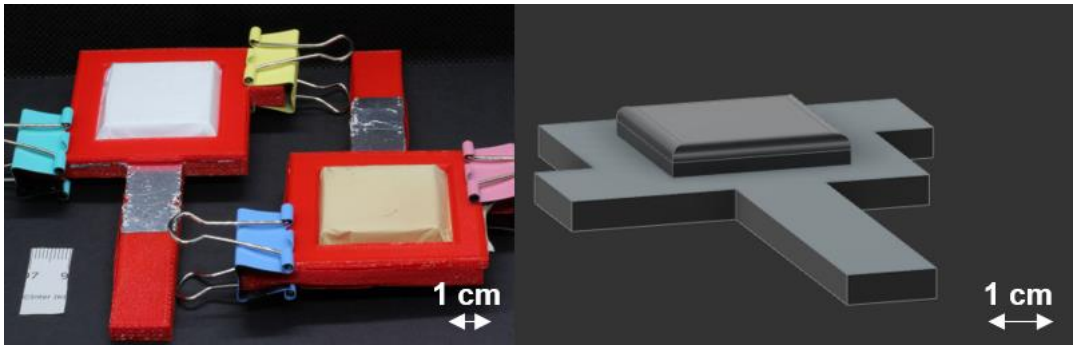

Figure A.8 — Manual triboelectric mechanism.

A.4.2 Gravitational triboelectric mechanism

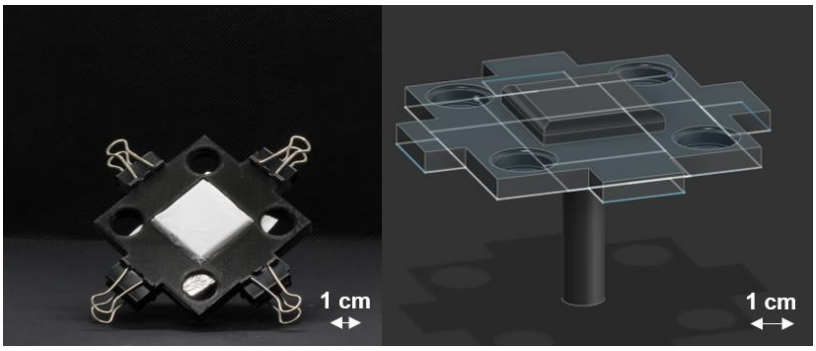

Figure A.9 — Moving membrane support in the gravitational triboelectric mechanism.

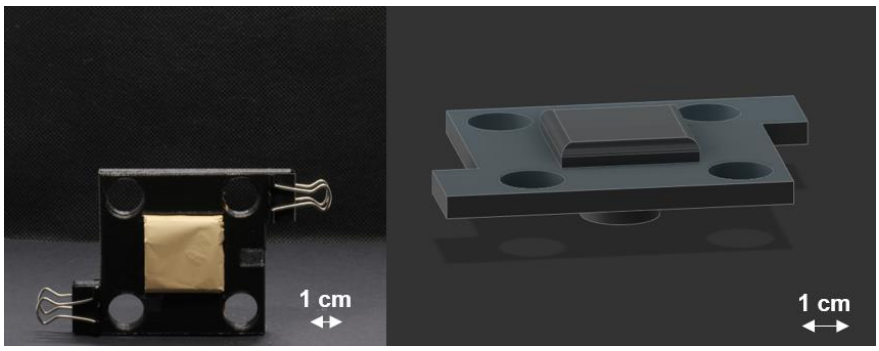

Figure A.10 — Static membrane support in the gravitational triboelectric mechanism.

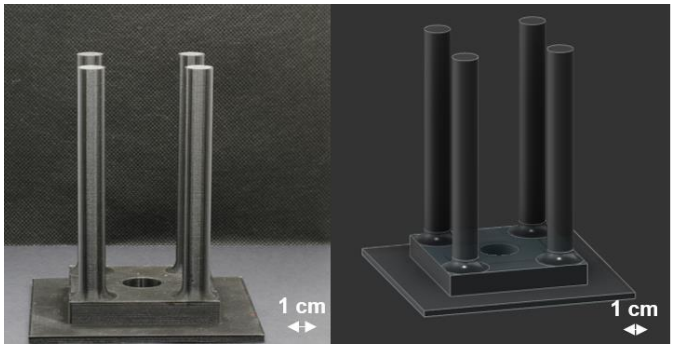

Figure A.11 — Support for static and moving membranes in the gravitational triboelectric mechanism.

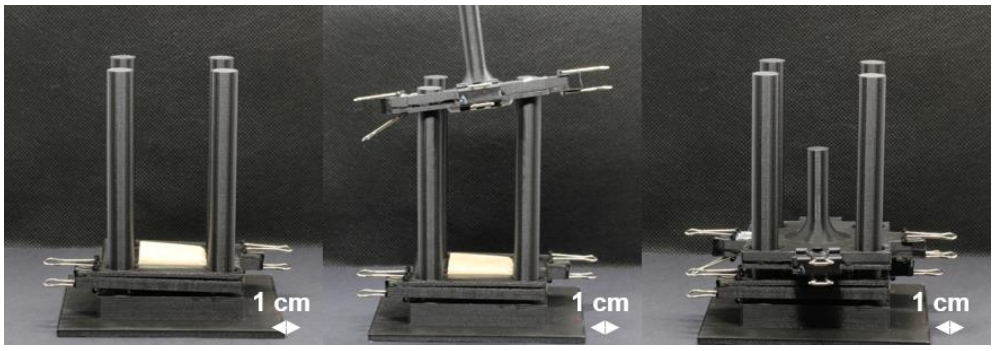

Figure A.12 — Gravitational triboelectric mechanism.

A.4.3 Jigsaw triboelectric mechanism

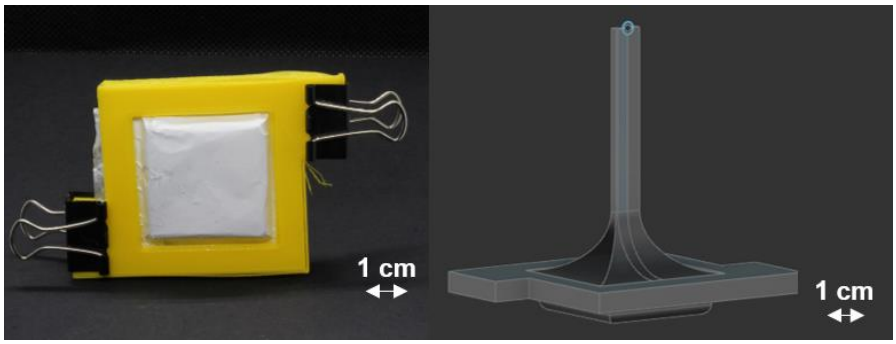

Figure A.13 — Moving membrane in the jigsaw triboelectric mechanism.

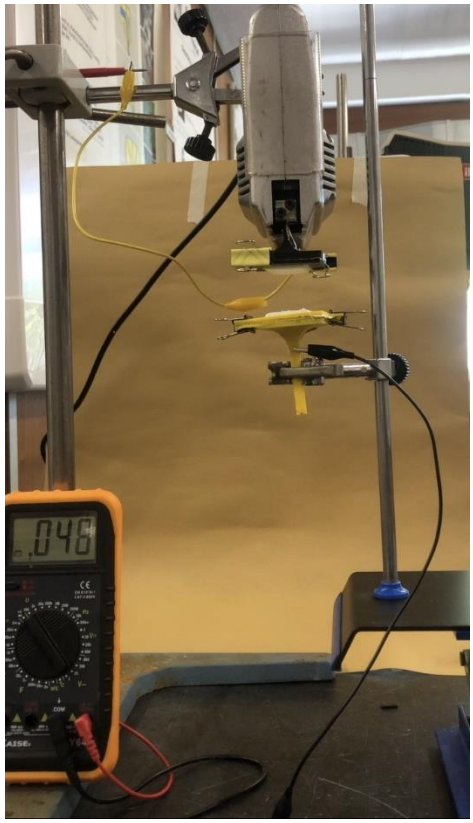

Figure A.14 — Jigsaw triboelectric mechanism.

A.4.4 Rotational triboelectric mechanism

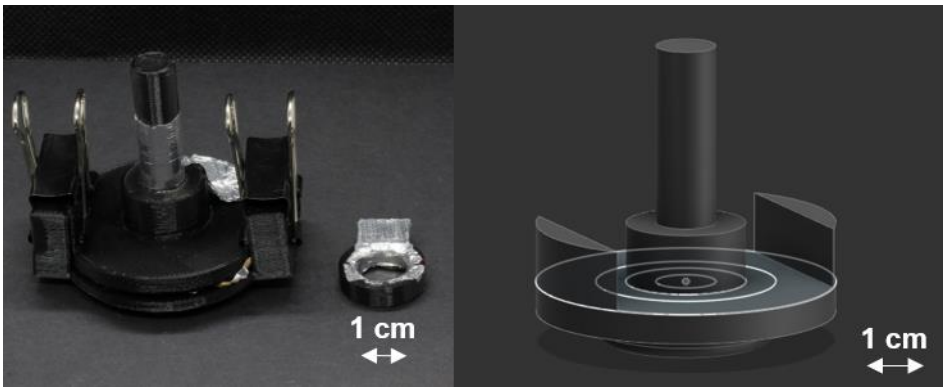

Figure A.15 — Rotatory membrane Moving membrane in the rotational triboelectric mechanism.

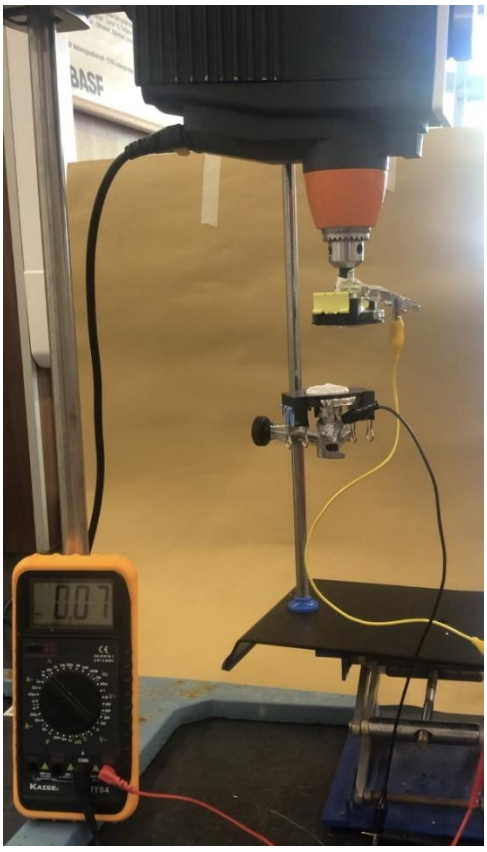

Figure A.16 — Rotational triboelectric mechanism.

A.5 Characterization of electrospun membranes and films

For the tensile tests, a previous preparation was made. The nine electrospun isotropic membranes were placed individually inside two sheets of parafilm, with the exception of PMMA which was set inside two sheets of aluminum foil. The reason PMMA membranes used aluminum foil instead of parafilm is because the polymeric fibers attached to the parafilm causing the disintegration of the

membranes. Later the membranes were cut into rectangular shape strips with 0.5-1 cm of width and 1.5-2 cm of length. A caliper was used to measure the membrane width and the L_o, and a micrometer for the membrane thickness. Having the membrane inside two sheets of parafilm or aluminum foil was to avoid damage resulting from the cutting and thickness measuring.

The triboelectric properties studied in the electrochemical tests required the use of 3D-printed objects. The first one used was the manual mechanism, in which the supports held two different 3 x 3 cm membranes. Connecting the contacts of the multimeter to each one of the membranes, the CS and LS modes were applied. This mechanism provided uncertain values of voltage and current values were not obtained. Since the manual mechanism had user error because of the variable force and duration applied to the membranes resulting in variable values, the gravitational mechanism was implemented. This mechanism consisted of two 3 x 3 cm membranes colliding with the same velocity and force every stroke. One membrane was dropped from a controlled height conserving the same force due to the gravitational force operating in the CS mode. In this mechanism, the membranes were connected to a potentiostat and values of V_{oc} and I_{sc} were obtained, being the most used to acquire all the results regarding randomly aligned electrospun membranes, bilayer composite electrospun membranes and films. To verify the effect of the high frequency of strokes the jigsaw mechanism was implemented. Applying the CS mode, one membrane was static and the other was connected to the jigsaw. Both with 9 cm^2 were linked to a multimeter and voltage values were obtained. The last mechanism was the rotational, in which two 7.07 cm^2 membranes were connected to a multimeter. In this mechanism, one membrane was static and the other was attached to a mechanical stirrer which provided a controlled rotation of the membrane, recreating the LS mode. One advantage of this mechanism is the possibility of controlling the rotation speed.

A.6 Surface morphology analysis of electrospun membranes

This section is dedicated to the additional acquired data relative to the surface morphology analysis of the electrospun membranes. In Figures 3.7 and 3.8, the SEM images of HPC and PVP were observed. With the objective of understanding the previous figures, Figure A.17 and Figure A.18, obtained through optical microscopy, are presented. Furthermore, in this section, macro-scale pictures of the electrospun membranes are presented in Figure A.19. The electrospun membranes presented a white color with the exception of the PVA membrane which displayed a yellow color.

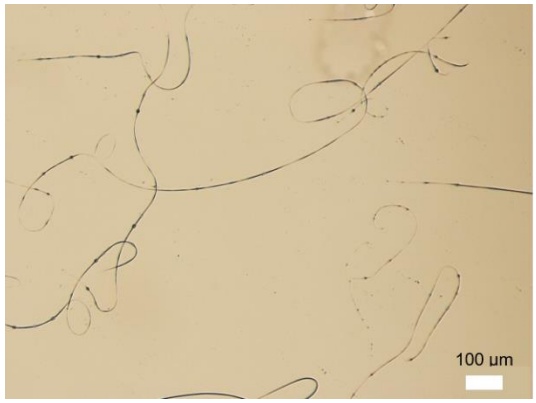

Figure A.17 — Optical microscopy image of HPC electrospun fibers.

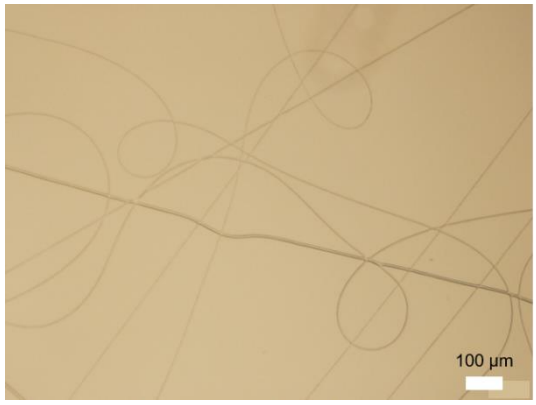

Figure A.18 — Optical microscopy image of PVP electrospun fibers.

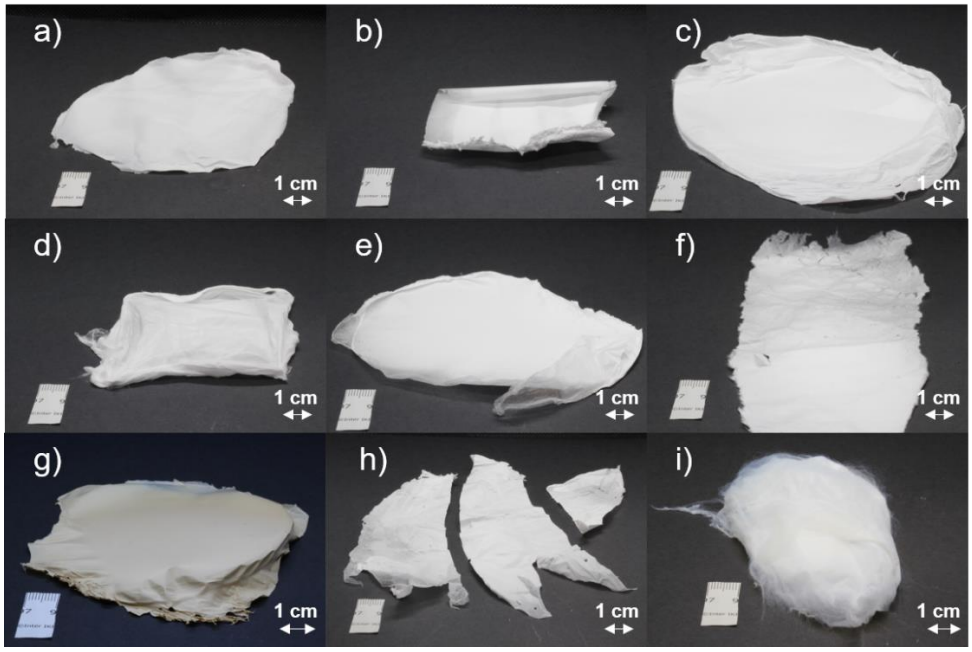

Figure A.19 — Macroscale pictures of the electrospun membranes, with a) PVDF; b) PVP; c) PMMA; d) PVDF-TRFE; e) PCL; f) CA; g) PVA; h) HPC; i) PS

Table A.3 — Values of Average Fiber Diameter with standard deviation obtained for the produced electrospun membranes.

Polymer	Average Fiber Diameter (µm)
CA	0.635 ± 0.281
PCL	1.347 ± 0.766
PS	3.379 ± 0.184
PMMA	0.593 ± 0.186
PVA	0.511 ± 0.324
PVDF	0.597 ± 0.400
PVDF-TRFE	0.786 ± 0.317
HPC	-
PVP	-

A.7 Chemical analysis of the electrospun membranes

Table A.4 — Values of Wavenumber and corresponding bonds for the produced electrospun membranes.

Polymer	Wavenumber (cm^{-1})								
	C-C	**C=C**	**C-H**	**C-O**	**C=O**	**C-O-C**	**O-H**	**C-Cl**	**C-F**
PVDF-TRFE	881	-	843	-	-	-	-	-	1400 1283 1178 1120
PCL	-	-	2943 2926 1471 1241 1188	1047	1723 1366	1294	-	732	-
PMMA	-	-	2957 1488 1437 1195 990	1242 1150	1731	-	-	-	-
HPC	-	-	2974 2882 1457	1376 1079	-	-	3457	-	-
CA	-	-	1371	1748 1238 1052	-	-	-	-	-
PVA	-	-	2943 1437	1334	1715	-	3369 1097	-	-
PVP	-	-	2925 1463 1423	-	1650	-	3381	-	-
PVDF	-	-	1073 879 841	-	-	-	-	-	1403 1276 1180
PS	-	1601	3000 1494 757	1060	-	-	-	-	-

A.8 Mechanical characterization of electrospun membranes

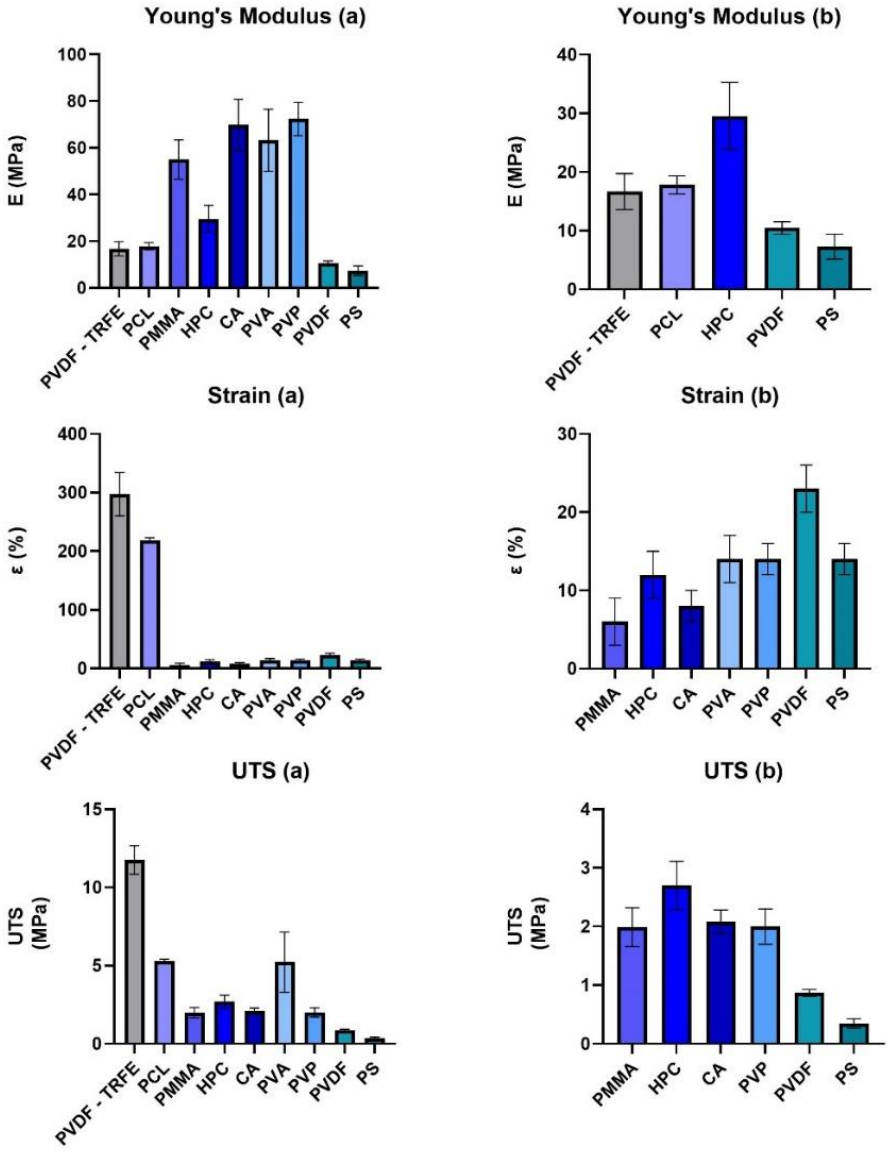

Figure A.20 — Comparison of the values of Young's Modulus, Strain and Ultimate Tensile Strength with standard deviation for the nine randomly aligned electrospun membranes. (a) all electrospun membranes; (b) magnified view.

A.9 Short circuit current - Electrospun membranes

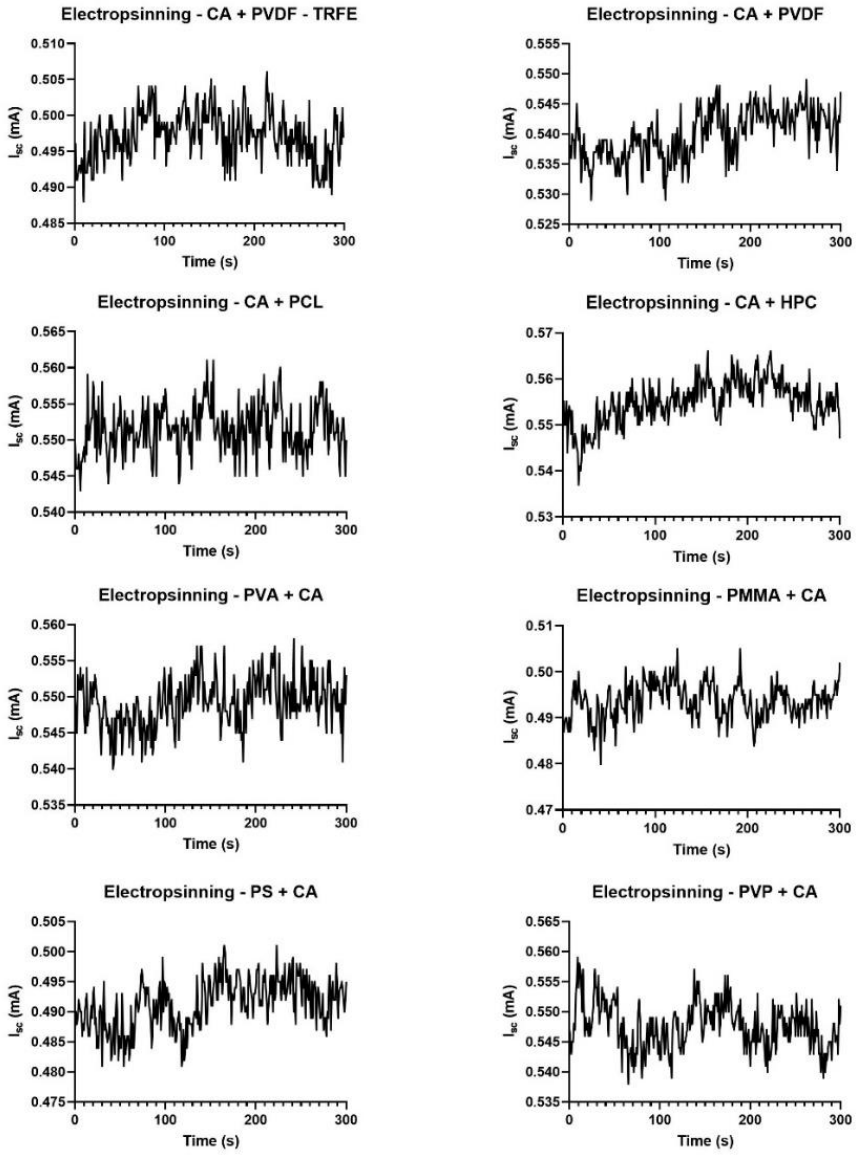

Figure A.21 — Short circuit current of electrospun membranes paired with CA.

A.10 Short circuit current - Films

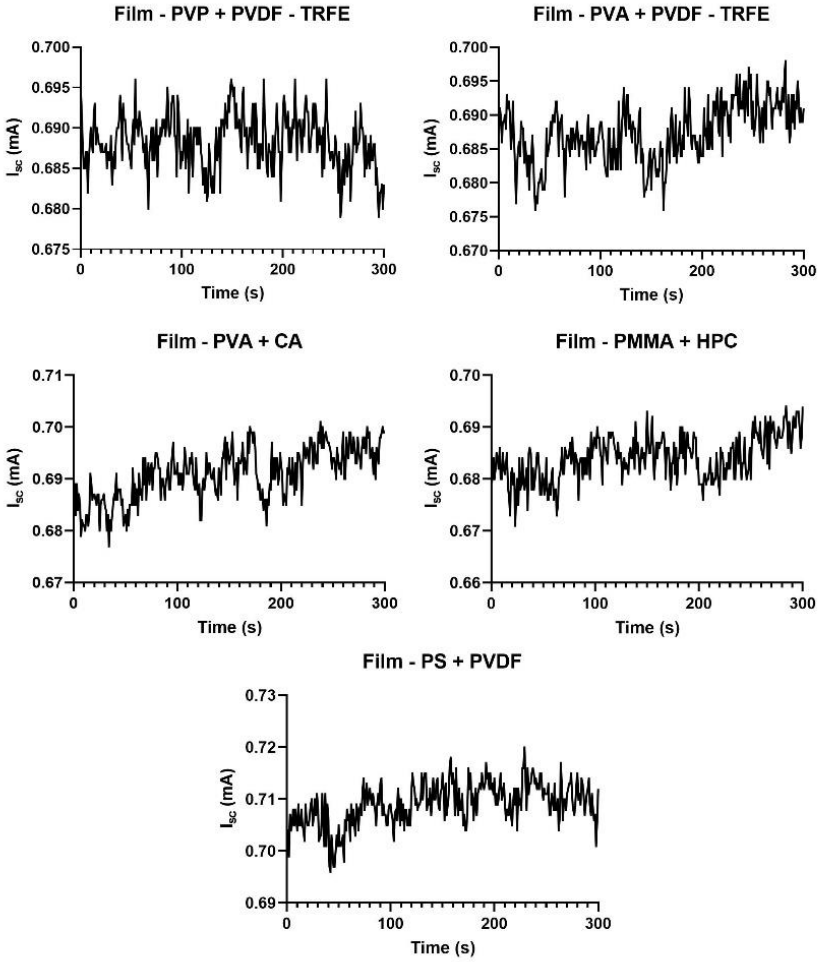

Figure A.22 — Short circuit current analysis of films.